Giant Metrewave Radio Telescope observations of X-shaped radio sources

Dharam Vir Lal* and A. Pramesh Rao

National Centre for Radio Astrophysics (NCRA-TIFR), Pune University Campus, Ganeshkhind, Pune 411 007, India

Accepted 2006 October 23. Received 2006 September 1; in original form 2006 May 12

ABSTRACT

We present results from a study of X-shaped sources based on observations using the Giant Metrewave Radio Telescope (GMRT). These observations were motivated by our low-frequency study of 3C 223.1, an X-shaped radio source, which showed that the wings (or low surface brightness jets) have flatter spectral indices than that of the active lobes (or high surface brightness jets), a result not easily explained by most models. We have now obtained GMRT data at 240 and 610 MHz for almost all the known X-shaped radio sources and have studied the distribution of the spectral indices across the sources. While the radio morphologies of all the sources at 240 and 610 MHz show the characteristic X-shape, the spectral characteristics of the X-shaped radio sources seem to fall into three categories, namely, sources in which (i) the wings have flatter spectral indices than the active lobes have, (ii) the wings and the active lobes have comparable spectral indices, and (iii) the wings have steeper spectral indices than the active lobes have. We discuss the implications of the new observational results on the various formation models that have been proposed for X-shaped sources.

Key words: galaxies: active – galaxies: formation – radio continuum: galaxies.

1 INTRODUCTION

A peculiar and a very small subclass of extragalactic radio sources called as the X-shaped or 'winged' sources are characterized by two low surface brightness lobes (the 'wings') oriented at an angle to the 'active', or high surface brightness radio lobes, giving the total source an 'X' shape. These two sets of lobes usually pass symmetrically through the centre of the associated host galaxy. Merritt & Ekers (2002) noted that the majority of these sources are of Fanaroff-Riley type II (FR II) (Fanaroff & Riley 1974) and the rest are either FR I or mixed.

X-shaped sources seem to reside in different types of host galaxies. Nearly half of these sources reside in fairly elliptical host galaxies. The hosts of some of these were reported to be slightly elongated and, in several prominent dust discs, have been found (Rottmann 2001). The environments of X-shaped sources seem to be poor. Almost all the sources are not part of rich clusters of groups. Rottmann (2001) reported five (NGC 326, 3C 223.1, 4C 48.29, B1059+169 3C 315 and 3C 403) of these sources to be located in galaxy groups or clusters. However, the density of these galaxy groups or clusters is low in all cases. The X-ray result shows that only one (NGC 326) is embedded in hot cluster gas, and this is the only source having a close companion galaxy.

Radio observations of these X-shaped sources show a high de-

gree of polarization (15-30 per cent) in the wings and an apparent

*E-mail: dharam@ncra.tifr.res.in

magnetic field structure parallel to the edge of the source and along the length of the wings (Dennett-Thorpe et al. 2002). Further, highfrequency and high-resolution radio polarization images showed field lines wrapping around the edges, as well as complex internal structure (3C 315, Högbom 1979; 3C 223.1, Black et al. 1992, etc.).

Several authors have attempted to explain the unusual structure in X-shaped sources. The first attempt was made by Rees (1978), who suggested that the jet direction precesses due to a realignment caused by the accretion of gas with respect to the central black hole axis. Dennett-Thorpe et al. (2002) discussed four possible scenarios for the formation of such radio morphology: (1) backflow from the active lobes into the wings (Leahy & Williams 1984; Capetti et al. 2002); (2) slow conical precession of the jet axis (Parma, Ekers & Fanti 1985; Mack et al. 1994); (3) reorientation of the jet axis during which flow continues; and (4) reorientation of the jet axis, but with the jet turned off or at greatly reduced power during the change of direction. Merritt & Ekers (2002) suggested another possible scenario, that is, the reorientation of black holes's spin axis due to a minor merger, leading to a sudden flip in the direction of any associated jet. A variant of Merritt & Ekers (2002) model was suggested by Gopal-Krishna, Biermann & Wiita (2003), where the sources with Z morphology within their X-shapes evolve along a Z-X morphological sequence. Presently, most of the observational results seem to prefer possibilities (3) and (4) of Dennett-Thorpe et al. (2002) or Merritt & Ekers (2002), and the key difference between these two models is in terms of mechanism of reorientation; the former favoured the disc-instability mechanism because of little evidence for recent merger, while the latter preferred the coalescence scenario. Nevertheless, in all these scenarios, the wings are interpreted as relics of past radio jets and the active lobes as the newer ones.

Lal & Rao (2005) presented an unusual result for 3C 223.1 source, that is, the wings (or low surface brightness jets) have flatter spectral indices with respect to the high surface brightness active lobes and this result is not easily explained in most models of the formation of X-shaped sources. Although unusual, it is a valuable result which puts stringent constraints on the formation models and nature of these sources. This unusual result for 3C 223.1 provides the motivation of this paper, that is, a systematic study of the sample of X-shaped sources using Giant Metrewave Radio Telescope (GMRT).

Furthermore, in this paper, we presented an 'alternative' formation scenario, which was not addressed earlier, that is, these sources consist of two pairs of jets, which are associated with two unresolved active galactic nuclei (AGNs). We also presented some of the assumptions used in the spectral ageing method for estimating the age, in order to explain the unusual result. Briefly, these are as follows. (1) The injection spectral index is varying (Palma et al. 2000). (2) In these sources, the low surface brightness wings are in the process of becoming new active jets. Hence, it is not surprising that they have flatter spectral index compared to that of the active lobes. (3) Presence of some exotic re-acceleration mechanism together with standard Alfven waves and Fermi mechanisms. (4) There is a gradient in magnetic field across the source, together with a curved electron energy spectrum, which would result in spectral indices being different at distinct locations within the source (Blundell & Rawlings 2000).

We present here the GMRT results from a systematic study of the sample of X-shaped radio sources at 240 and 610 MHz. In Section 3, we describe the observations of the sample, data reduction (Section 4) and present the images derived from the GMRT at 240 and 610 MHz along with distribution of low-frequency, 240–610 MHz spectra across all these sources (Section 5). We also interpret our results, combine our data with previously published data for all of these sources, and discuss the statistical implications of these results on the formation models (Section 6). We summarize the salient conclusions of our study in Section 7.

2 SAMPLE

The sample is drawn from the list of X-shaped sources mentioned in Merritt & Ekers (2002) compiled by Leahy & Parma (1992). The

sources have been selected solely on the basis of their morphology. 3C 192 was classified as an X-shaped source Parma et al. (1985), but was not included in the list of all such known sources (Merritt & Ekers 2002), and we have included it in our sample. However, it is important to note that the images on which the selection was based have been obtained with various instruments and with vast differences in sensitivity and resolution. Therefore, the sample of these 12 sources is inhomogeneous and in no sense a statistically complete sample.

3 OBSERVATIONS

We adopted an observing strategy similar to our earlier observations for 3C 223.1 (Lal & Rao 2005). The 240- and 610-MHz feeds of the GMRT are coaxial feeds and, therefore, simultaneous dual-frequency observations at these two frequencies were performed. The primary beams are ~108 and ~43 arcmin at 240 and 610 MHz, respectively. We made full synthesis observations of all the X-shaped sources, 240 and 610 MHz, in the dual-frequency mode, using the GMRT in the standard spectral line mode with a spectral resolution of 125 kHz. These sources were observed in two cycles (03DVL01: four out of the 11 and 05DVL01: seven out of the 11 sources). Table 1 gives the details of the observations. Since NGC 326 is already observed using the GMRT at low frequencies, we did not perform new observations.

The GMRT has a hybrid configuration (Swarup et al. 1991) with 14 out of its 30 antennas located in a central compact array with size ~1.1 km and the remaining antennas distributed in a roughly 'Y'-shaped configuration, giving a maximum baseline length of ~25 km. The baselines obtained from antennas in the central square are similar in length to the Very Large Array (VLA) D-array, while the baselines between the arm antennas are comparable in length to the VLA B-array. Hence, a single observation with the GMRT provides both, that is, it samples the ultraviolet (UV) plane adequately on the short baselines as well as on the long baselines and provides good angular resolution when mapping the detailed source structure with reasonably good sensitivity.

4 DATA REDUCTION

The visibility data were converted to FITS and analysed using standard AIPS. The flux calibrators 3C 48, 3C 147 and 3C 286 were observed depending on the availability either at the beginning or

Table 1. The observing log for all the observed X-shaped sources.

	Right ascension Declination		Observing	Bandwidth		Centre	Calibrator		$t_{\rm integration}$
	(J20	00)	date	Nominal	Effective	frequency (610 MHz/240 MHz)	flux	phase	(onsource) (h)
4C 12.03	00:09:52.6	+12:44:04.9	2003 December 18	16/8	13.5/6	606.44/237.69	3C 286	0054-035	4.97
3C 52	01:48:29.0	+53:32:35.4	2003 January 12	16/8	14.25/5	606.68/240.56	3C 286	0110+565 0114+483	6.29
3C 136.1	05:16:03.1	+24:58:25.5	2003 January 9	16/8	14.25/6.75	606.68/240.06	3C 286	0521 + 166	5.65
3C 192	08:05:35.0	+24:09:50.0	2004 April 10	16/6	13.125/5.625	606.31/240.19	3C 48	0804 + 102	6.38
B2 0828+32	08:31:27.5	+32:19:26.4	2003 December 18	16/8	13.125/5	606.31/236.44	3C 48	0909 + 428	6.94
3C 223.1	09:41:24.0	+39:44:41.9	2003 December 18	16/8	14.25/5	606.68/237.19	3C 286	0834 + 555	6.67
4C 48.29	10:20:53.6	+48:31:24.3	2004 April 11	16/6	13.875/5	606.44/240.12	3C 147	0834+555	6.42
B1059+169	11:01:33.0	+16:43:52.0	2004 February 8	16/8	13.5/6	606.25/240.06	3C 286	1021 + 219	5.33
3C 315	15:13:40.1	+26:07:31.2	2003 January 10	8/6	6.375/5	610.13/237.19	3C 286	1506+375	5.89
3C 403	19:52:15.8	+02:30:24.5	2003 December 18	16/8	13.5/6.25	606.37/236.94	3C 48	1941 - 154	4.97
3C 433	21:23:44.5	+25:04:11.9	2003 January 13	8/6	6.375/5.625	610.13/240.75	3C 286	2225-049 2052+365	5.05

at the end as an amplitude calibrator to estimate and correct for the bandpass shape. We used the flux density scale which is an extension of the Baars et al. (1977) scale to low frequencies, using the coefficients in the AIPS task 'SETJY'. The secondary phase calibrator was observed at intervals of 35 min. The error in the estimated flux density, both due to calibration and due to systematic, is \lesssim 5 per cent. The data suffered from scintillations and intermittent radio frequency interference (RFI). In addition to normal editing of the data, the scintillations affected data, and channels affected due to RFI were identified and edited, after which the central channels were averaged using the AIPS task 'SPLAT' to reduce the data volume. To avoid bandwidth smearing, effective band at 240 and 610 MHz was reduced to five and three channels, respectively.

While imaging, 49 facets spread across a \sim 1°.8 \times 1°.8 field were used at 240 MHz and nine facets covering slightly less than a 0°.7 \times 0°.7 field were used at 610 MHz to map each of the two fields using the AIPS task 'IMAGR'. In order to achieve high-resolution images that are also sensitive to extended structure, we have employed the Steer, Dewdney & Ito CLEANing algorithm (Steer, Dewdney & Ito 2003). We used a 'uniform' weighting and the 3D option for W term correction throughout our analysis. The presence of a large

number of point sources in the field allowed us to do phase self-calibration to improve the image. After two to three rounds of phase self-calibration, a final self-calibration of both amplitude and phase was made to get the final image. At each round of self-calibration, the image and the visibilities were compared to check for the improvement in the source model. The final maps were combined using the AIPS task 'FLATN' and corrected for the primary beam of the GMRT antennas.

5 RESULTS

The radio images shown in Figs 1–11 have nearly complete UV coverage, angular resolutions of \sim 12 and \sim 5 arcsec and the rms noise in the maps is in the range \sim 1.0–6.9 and \sim 0.2–0.8 mJy beam⁻¹ at 240 and 610 MHz, respectively. The dynamic ranges in the maps are in the range 900–2000 and 1700–5000 at 240 and 610 MHz, respectively. Consequently, in the vicinity of strong sources, including the sources discussed here, the local noise was sometimes higher than the noise in empty regions. The selection of contours shown in the figures is based on the rms noise in the immediate vicinity of the source, with first contour level being three to five times this rms

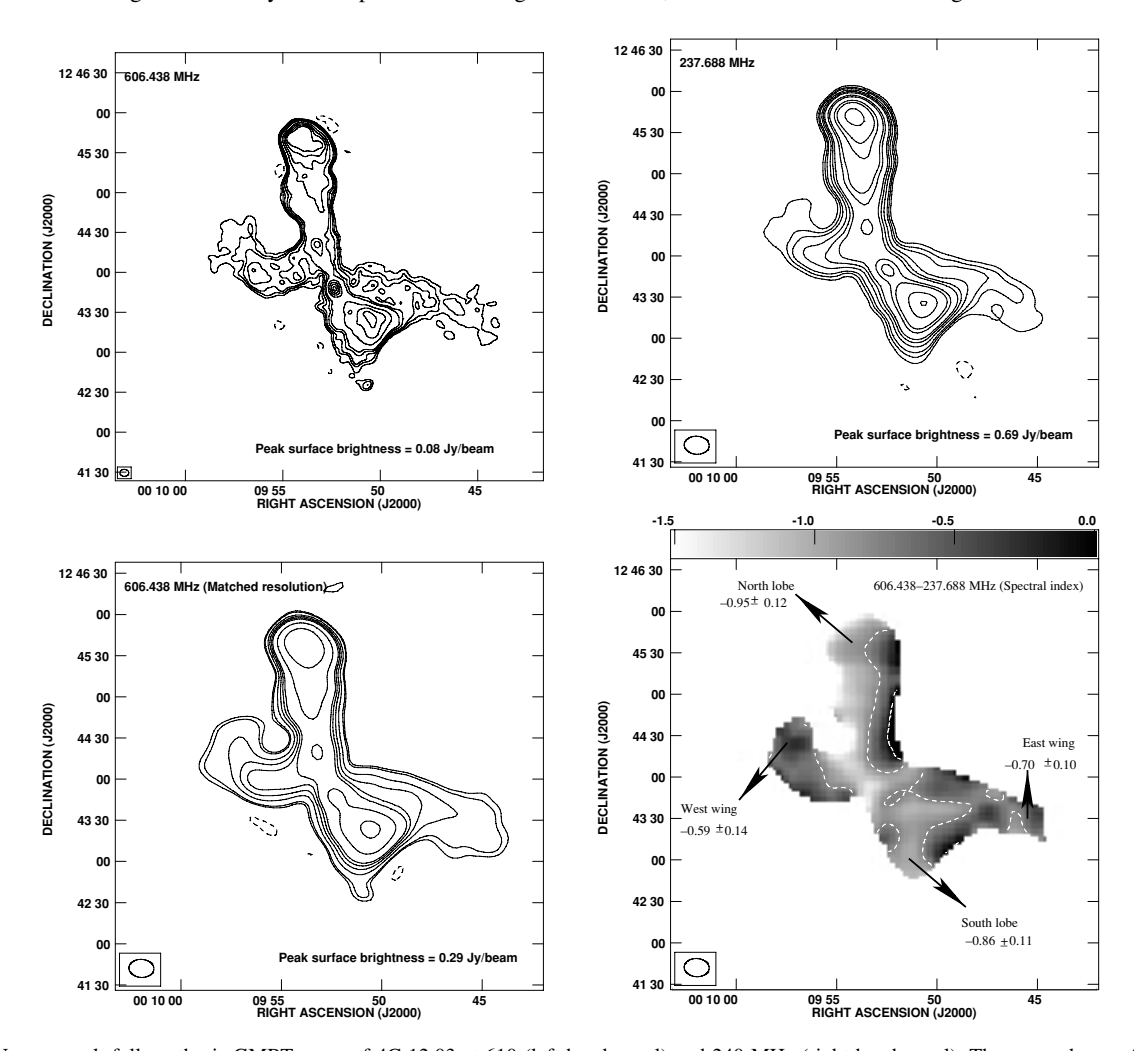


Figure 1. Upper panel: full synthesis GMRT maps of 4C 12.03 at 610 (left-hand panel) and 240 MHz (right-hand panel). The CLEAN beams for 610- and 240-MHz maps are 6.7×5.5 arcsec² at a position angle (PA) of 89.8 and 18.2×13.1 arcsec² at a PA of 86.4, respectively, and the contour levels in the two maps are, respectively, -2, 2, 3, 4, 6, 8, 16, 24, 32, 40 and -20, 20, 30, 40, 60, 80, 100, 160, 200, 320, 400 mJy beam⁻¹. Lower left-hand panel: the map of 4C 12.03 at 610 MHz matched with the resolution of 240 MHz. The contour levels are -6, 6, 8, 16, 24, 32, 40, 80, 160 mJy beam⁻¹. Lower right-hand panel: the distribution of the spectral indices, between 240 and 610 MHz, for the source. The spectral index contours are at -0.8, 0. The error bars in the full synthesis maps found at a source-free location are ~ 2.0 and ~ 0.3 mJy beam⁻¹ at 240 and 610 MHz, respectively.

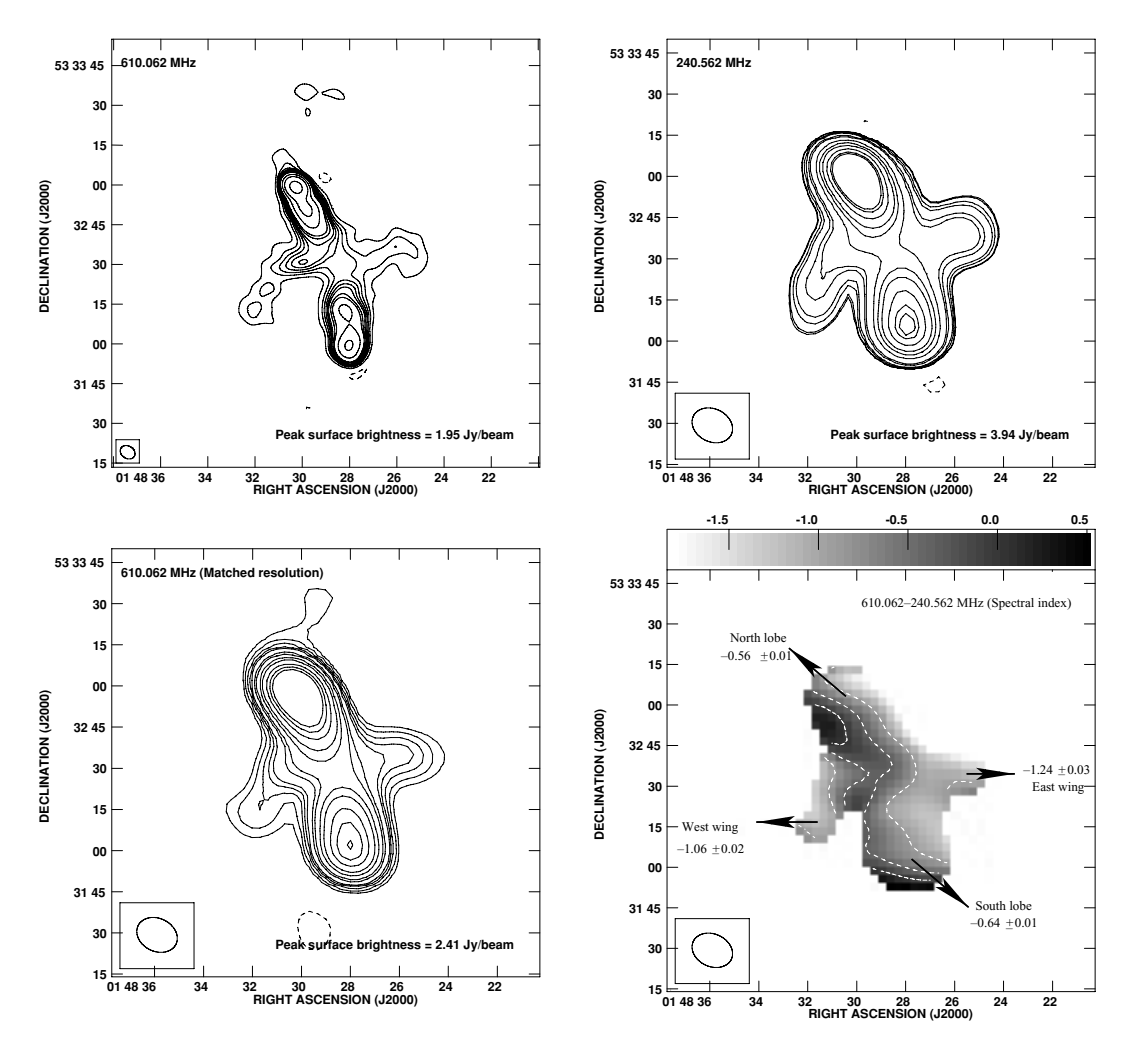


Figure 2. Upper panel: full synthesis GMRT maps of 3C 52 at 610 (left-hand panel) and 240 MHz (right-hand panel). The CLEAN beams for 610- and 240-MHz maps are $5.9 \times 4.7 \, \mathrm{arcsec^2}$ at a PA of $57^\circ.5$ and $15.4 \times 12.0 \, \mathrm{arcsec^2}$ at a PA of $63^\circ.7$, respectively, and the contour levels in the two maps are, respectively, $-8, 8, 20, 30, 40, 50, 60, 80, 100, 200 \, \mathrm{and}$ $-50, 50, 60, 80, 100, 160, 200, 400, 600, 800, 1200, 1600, 1800 \, \mathrm{mJy}$ beam⁻¹. Lower left-hand panel: the map of 3C 52 at 610 MHz matched with the resolution of 240 MHz. The contour levels are $-24, 24, 40, 60, 80, 100, 160, 200, 300, 400, 600, 800 \, \mathrm{mJy}$ beam⁻¹. Lower right-hand panel: the distribution of the spectral indices, between 240 and 610 MHz, for the source. The spectral index contours are at -0.9, -0.4, 0. The error bars in the full synthesis maps found at a source-free location are ~ 1.4 and ~ 0.3 mJy beam⁻¹ at 240 and 610 MHz, respectively.

noise. To make further comparisons of the morphology and flux densities, the final calibrated UV data at 610 MHz were mapped using a UV taper of 0–22 k λ , which is similar to that of 240-MHz data and then restored using the restoring beam corresponding to the 240-MHz map. The full synthesis 610- and 240-MHz contour maps and the 610-MHz matched resolution contour map for all the observed sources are shown in Figs 1–11. The sequence of maps is ordered in right ascension (RA). An ellipse in a box in the lower left-hand corner of each map shows the shape of the synthesized beam [full width at half-maximum (FWHM)]. All positions are given in J2000 coordinates.

5.1 Radio morphology and low-frequency radio spectra

The first high angular resolution, high-sensitivity images of X-shaped sources at the lowest frequencies of 240 MHz (upper right-hand panels) and 610 MHz (upper left-hand panels) are shown in Figs 1–11. In all the sources, the radio morphologies at 240 and 610 MHz show well-defined X-shape with a pair of active jets and a pair of wings, that pass symmetrically through the position of the parent galaxy. Table 2 lists the integrated flux densities of all

the sources along with previous measurements at other frequencies and are plotted in Fig. 12. Our estimates at both frequencies, 240 and 610 MHz, agree well with that of the measurements from other instruments. We therefore believe that we have not lost any flux density in our interferometric observations and there are no systematics introduced in our analysis.

The observations and morphologies described allow us to investigate in detail the spectral index distributions of all sources. The restored and matched maps at 240 and 610 MHz were used further for the spectral analysis for each of these sources. We determine the spectral index distribution using the standard direct method of determining the spectral index between maps $S_{\nu_1}(x, y)$ and $S_{\nu_2}(x, y)$ at two frequencies ν_1 and ν_2 , and is given by the ratio of $\log(S_{\nu_1}(x, y)/S_{\nu_2}(x, y))$ and $\log(\nu_1/\nu_2)$.

The flux densities at 240 and 610 MHz plotted in Fig. 12 are calculated using the images shown in Figs 1–11 (upper right-hand and lower left-hand panels), which are matched to the same resolution, and these values are tabulated in Tables 2 and 3. The flux densities for the active lobes and the wings are integrated over the region, which is at least four times the beam size (a circular region of \sim 5 pixel radius centred at the position of the tail of the arrows shown

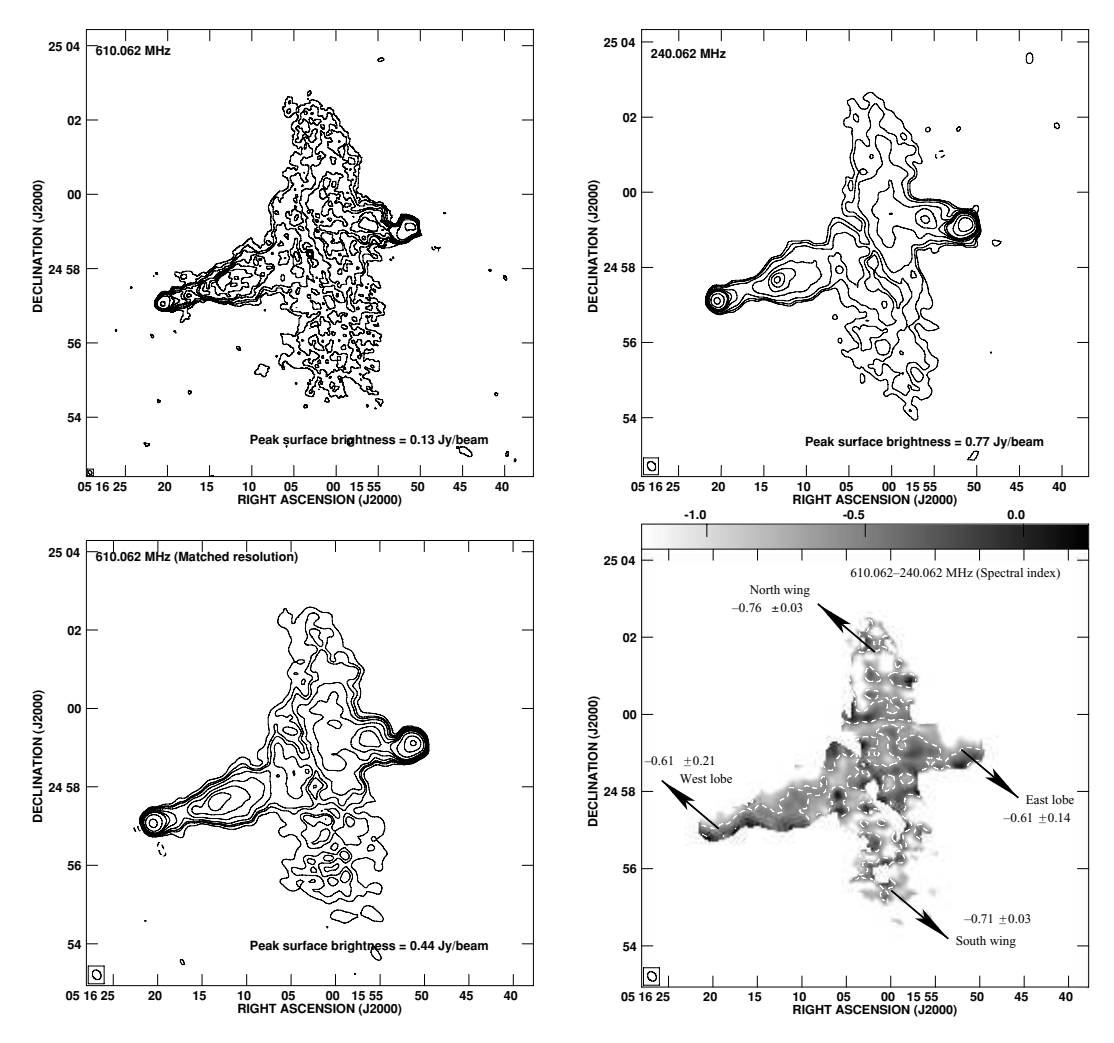


Figure 3. Upper panel: full synthesis GMRT maps of 3C 136.1 at 610 (left-hand panel) and 240 MHz (right-hand panel). The CLEAN beams for 610- and 240-MHz maps are $6.7 \times 5.1 \,\mathrm{arcsec^2}$ at a PA of $28^{\circ}.2 \,\mathrm{and}$ $15.5 \times 12.3 \,\mathrm{arcsec^2}$ at a PA of $32^{\circ}.7$, respectively, and the contour levels in the two maps are, respectively, $-1.6 \, 1.6, 2.4, 3.2, 4.8, 6, 8, 10, 20, 80 \,\mathrm{and}$ $-8, 8, 12, 20, 40, 60, 80, 100, 200, 400 \,\mathrm{mJy}$ beam⁻¹. Lower left-hand panel: the map of 3C 136.1 at 610 MHz matched with the resolution of 240 MHz. The contour levels are $-3, 3, 6, 8, 12, 20, 30, 40, 80, 200, 400 \,\mathrm{mJy}$ beam⁻¹. Lower right-hand panel: the distribution of the spectral indices, between 240 and 610 MHz, for the source. The spectral index contours are at -0.6, 0.2. The error bars in the full synthesis maps found at a source-free location are $\sim 1.2 \,\mathrm{and} \sim 0.2 \,\mathrm{mJy}$ beam⁻¹ at 240 and 610 MHz, respectively. The white patches in the spectral index map seen in the wings are steep spectrum features and is due to slightly higher noise cut-off.

using the AIPS task 'IMEAN') and above their 3σ contour to reduce statistical errors. In addition, we have used conservative estimates of error bars on the flux densities at each location. These estimates were determined from the fluctuations in the region being averaged and not from the noise at a source-free location using a similar-sized circular region, which being much smaller (see the figure captions). These error bars, both spectral indices and flux densities, do not change significantly with increasing or decreasing the size of circle, and also they do not change significantly by changing slightly the position of circular region. Furthermore, we have also examined the possibility that (i) the different UV coverages, (ii) the negative depression around the source, and (iii) the image misalignments at 240 and 610 MHz could produce some systematic errors. The former seems unlikely since the GMRT has good UV coverage, and sources are only \sim 3-4 arcmin across and are much smaller than the short baseline lengths of \sim 35 arcmin (\simeq 100 wavelengths) at 610 MHz and \sim 100 arcmin (\simeq 35 wavelengths) at 240 MHz. Nevertheless, we Fourier transform the 240-MHz CLEAN map, sampling it with the UV coverage of 610 MHz and re-imaging this visibility data set. The

resultant map showed no systematic differences from the original 240-MHz map and the rms difference in the two maps was less than 4 per cent, corresponding to the rms error in the spectral index of \lesssim 0.05. Furthermore, 240-MHz maps of two sources (Fig. 6: 3C 223.1 and Fig. 11: 3C 433) show marginal evidence that these images contain a negative depression around them. A negative depression/bowl is seen in a synthesis image either due to inadequate UV coverage at short baseline lengths or due to inadequate CLEANing. The former being unlikely as explained above, we examine the latter. While imaging, we did not provide zero-spacing flux density, but we have done deep CLEANing, so as not to make any deconvolution errors. Comparisons of expected integrated flux density, total CLEANed flux density and flux density measured by short baseline lengths suggest no discrepancy beyond 5 per cent. In any case, we quantify the errors that would be introduced due to possible negative depression for these two sources below. Finally, in each case, we not only registered the target source, but the positions of at least five field sources around the X-shaped source, which were common in the two maps, were also registered, and alignment of the two

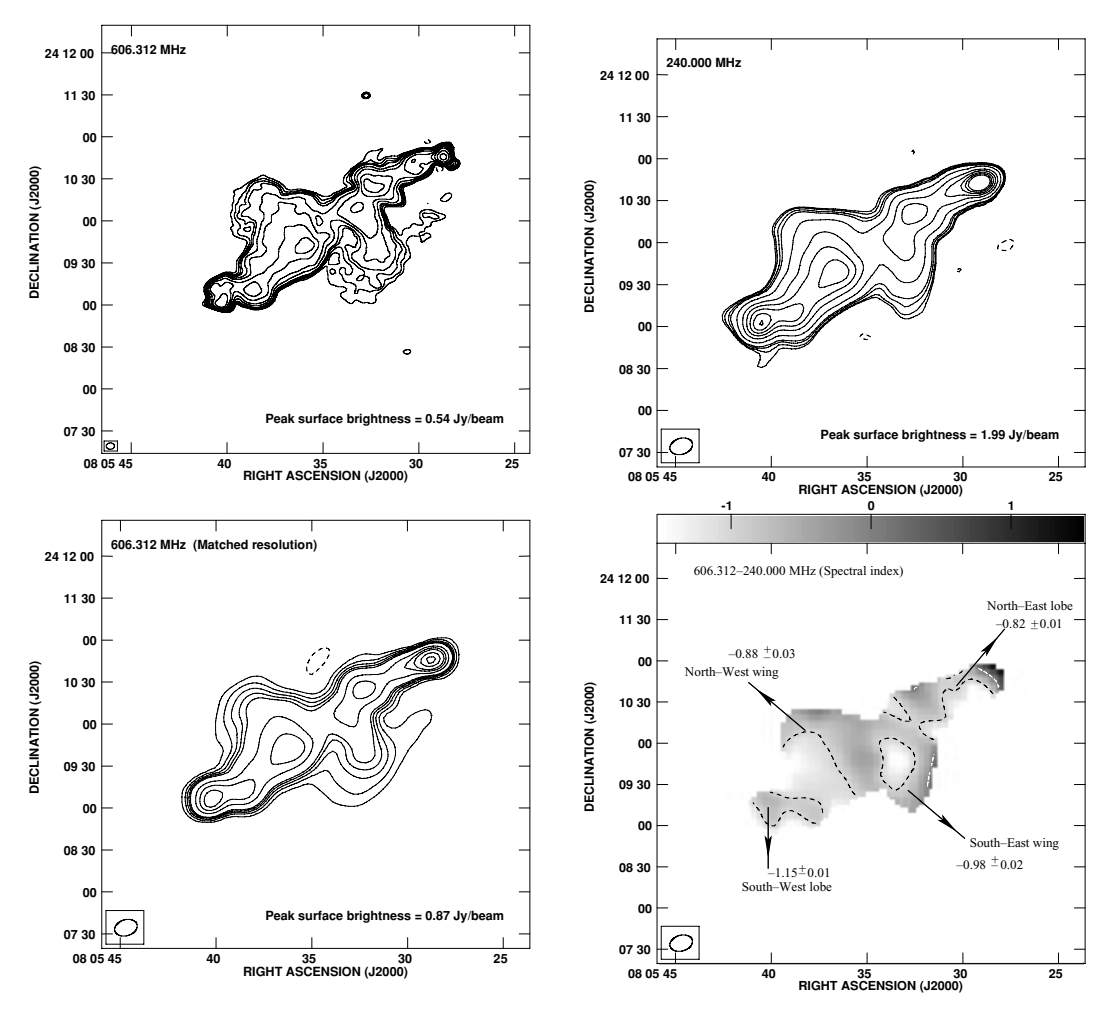


Figure 4. Upper panel: full synthesis GMRT maps of 3C 192 at 610 (left-hand panel) and 240 MHz (right-hand panel). The CLEAN beams for 610- and 240-MHz maps are 6.0×4.5 arcsec² at a PA of $-88^{\circ}1$ and 16.5×11.5 arcsec² at a PA of $-73^{\circ}2$, respectively, and the contour levels in the two maps are, respectively, -4, 4, 6, 8, 10, 16, 24, 40, 60, 80, 100 and -50, 50, 60, 80, 100, 200, 400, 600, 80 1000 mJy beam⁻¹. Lower left-hand panel: the map of 3C 192 at 610 MHz matched with the resolution of 240 MHz. The contour levels are -20, 20, 40, 60, 80, 100, 200, 300, 400, 600, 800, 1000 mJy beam⁻¹. Lower right-hand panel: the distribution of the spectral indices, between 240 and 610 MHz, for the source. The spectral index contours are at -1, 0. The error bars in the full synthesis maps found at a source-free location are \sim 2.4 and \sim 0.5 mJy beam⁻¹ at 240 and 610 MHz, respectively.

images is better than 15 per cent. Therefore, in order to understand the nature of X-shaped sources, we take into account our careful analyses and estimation of the possible systematic errors.

Analyses of the spectrum, shown in Figs 1–11 (lower right-hand panels), in different regions of each of these sources show remarkable variation across them. The lighter regions represent the relatively steep spectrum as compared to the darker regions which represent flat spectrum. Although the full range of spectral indices is large, we have shown only a small range for clarity in each case. We now describe the radio structure of X-shaped radio sources measured by the GMRT along with the best power-law fit $(S_{\nu} \propto \nu^{\alpha})$ for several regions across the source. Here, we also include the description of 3C 223.1 (Lal & Rao 2005) and NGC 326 (Murgia et al. 2001), published in the literature.

(i) NGC 326 (z = 0.047). This galaxy is the brightest member of the Zwicky cluster 0056.9+2636 (Zwicky & Kowal 1968). The host is a dumbbell-shaped galaxy with clearly separated nuclei (Wirth, Smarr & Gallagher 1982).

NGC 326 was the first X-shaped radio source discovered (Ekers et al. 1978). At 1.4 GHz, the lobes are slightly resolved

and the most-prominent components are the two wings. The lobes are asymmetric in total emission, extent and distance from the core. The southern lobe has an ellipsoidal shape, while the northern lobe is more elongated and wider (Murgia et al. 2001). The wings bend and extend away from the lobe axis by \sim 2 arcsec. Furthermore, the overall Z-shape symmetry is broken by the low surface brightness plume located just above the end of the east wing (Worrall, Birkinshaw & Cameron 1995).

In the east wing, there is a monotonic steepening of the radio spectrum from the south lobe to the end of the wing; the spectral index distributions between 1.4 and 4.8 GHz and between 4.8 and 8.5 GHz decrease from -0.6 and -0.7 to -1.3 and -1.9, respectively, whereas in the west wing, the spectral index distributions between 1.4 and 4.8 GHz and between 4.8 and 8.5 GHz decrease, respectively, from -0.6 and -0.7 to -1.3 and -1.5 (Murgia et al. 2001). Similarly, in the south lobe the spectral index distribution between 1.4 and 4.8 GHz is roughly constant around a value of 0.6 and the spectral index distribution between 4.8 and 8.5 GHz decreases from -0.7 to -1.3, whereas in the north lobe the spectral index distributions between 4.8 and between 4.8 and

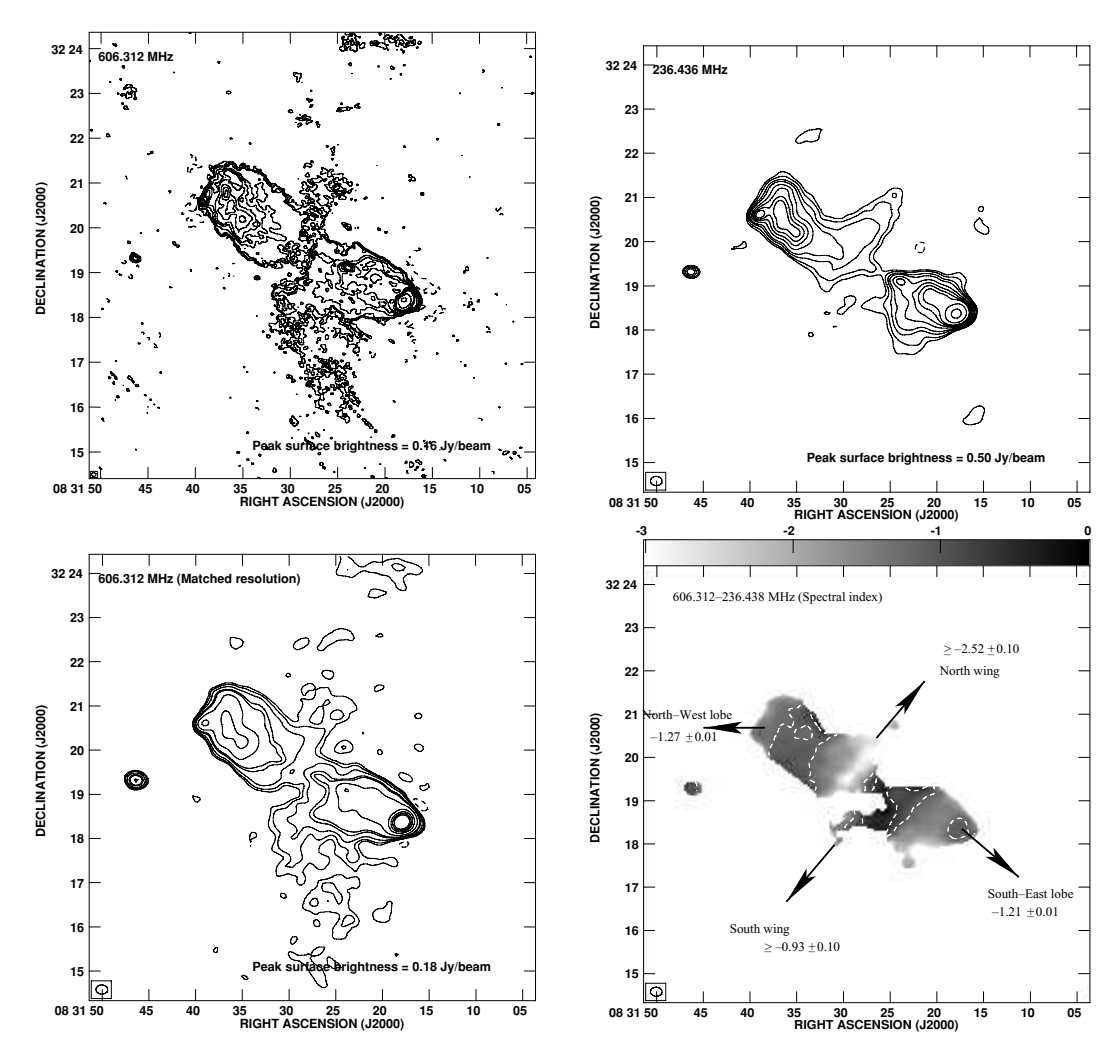


Figure 5. Upper panel: full synthesis GMRT maps of B2 0828+28 at 610 (left-hand panel) and 240 MHz (right-hand panel). The CLEAN beams for 610-and 240-MHz maps are $6.0 \times 4.8 \,\mathrm{arcsec^2}$ at a PA of $81^\circ 9$ and $15.8 \times 12.5 \,\mathrm{arcsec^2}$ at a PA of $89^\circ 2$, respectively, and the contour levels in the two maps are, respectively, -1, 1, 2, 3, 4, 6, 8, 10, 20, $40 \,\mathrm{and} -14$, 14, 20, 30, 40, 50, 80, 100, 120, 200, $400 \,\mathrm{mJy} \,\mathrm{beam^{-1}}$. Lower left-hand panel: the map of B2 0828+28 at 610 MHz matched with the resolution of 240 MHz. The contour levels are -1, 1, 2, 4, 8, 10, 20, 30, 40, 60, 80, $100 \,\mathrm{mJy} \,\mathrm{beam^{-1}}$. Lower right-hand panel: the distribution of the spectral indices, between 240 and 610 MHz, for the source. The spectral index contours are at -1.2, -0.7, 0. The error bars in the full synthesis maps found at a source-free location are $\sim 2.7 \,\mathrm{and} \sim 0.2 \,\mathrm{mJy} \,\mathrm{beam^{-1}}$ at 240 and 610 MHz, respectively.

 $8.5~\mathrm{GHz}$ increase, respectively, from $-0.75~\mathrm{and}~-1.35~\mathrm{at}$ the lobe head to $-0.65~\mathrm{and}~-0.8$ and become $-1.0~\mathrm{and}~-1.6$ in proximity of the core (Murgia et al. 2001). Briefly, the active lobes have flatter $1.4–8.5~\mathrm{GHz}$ spectral index as compared to the wings and the $0.325-1.4~\mathrm{GHz}$ spectra also show similar behaviour (private communication).

(ii) $4C\ 12.03$ (z=0.110). $4C\ 12.03$ is associated with an elliptical host galaxy (Heckman et al. 1994) and has been classified as a low emission line radio galaxy (Laing, Riley & Longair 1983). Morphologically, $4C\ 12.03$ seems to lie at the FR I/FR II division, whereas the radio luminosity suggests it to be an FR I source.

Fig. 1 at 240 and 610 MHz shows symmetrical structure and extent in the two matched resolution radio maps, as is usually the case for radio galaxies. The northern jet leading to the north hotspot possibly consists of the active axis and the other axis, that is, the eastwest axis consists of the wings. The source has an angular extent of $3.8 \times 4.0 \, \mathrm{arcmin^2}$ in both 240- and 610-MHz maps.

The high-frequency spectral index distribution between 1.5 and 10.45 GHz at a resolution of $69 \times 69\,\mathrm{arcsec^2}$ shows a marginal steepening from the active lobes ($\alpha \simeq -0.8$) to the wings ($\alpha \simeq -1.0$) (Rottmann 2001). The low-frequency fitted spectra have $-0.59 > \alpha > -0.95$ for all regions across the source. Contrary to the high-frequency spectral results, the low-frequency result shows definite evidence for steeper spectra in the active lobes than in the wings, and the east and west wings have spectral indices -0.70 ± 0.10 and -0.59 ± 0.14 , respectively, whereas the north and south active lobes have -0.95 ± 0.12 and -0.86 ± 0.11 , respectively.

(iii) 3C52 (z = 0.285). 3C52 is the most-distant X-shaped source. An *HST* imaging by de Koff (1996) showed the galaxy to be elongated along the north–south axis and it shows a pronounced dust disc.

Fig. 2 shows the radio images at 240 and 610 MHz. The core is undetected in low-resolution radio maps, but a closer inspection of radio contours in the 610-MHz map shows presence of possible core at the position of parent galaxy. Historically, this source is an

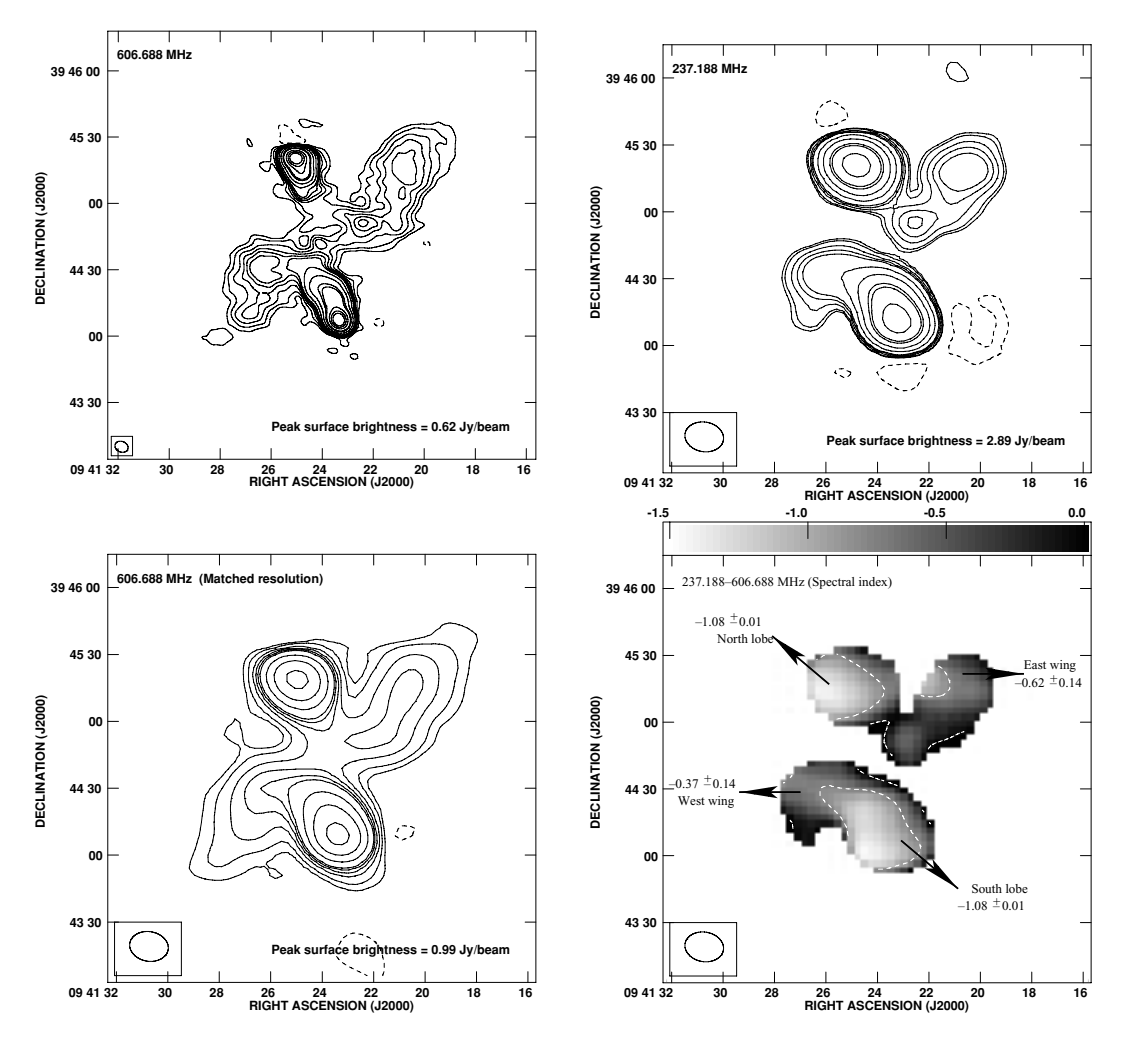


Figure 6. Upper panel: full synthesis GMRT maps of 3C 223.1 at 610 (left-hand panel) and 240 MHz (right-hand panel). The CLEAN beams for 610- and 240-MHz maps are $6.1 \times 4.8 \,\mathrm{arcsec^2}$ at a PA of $66^\circ.8$ and $17.4 \times 13.3 \,\mathrm{arcsec^2}$ at a PA of $80^\circ.3$, respectively, and the contour levels in the two maps are, respectively, -2, 2, 4, 6, 8, 10, 12, 20, 40, 80, 100, 200, 300, $400 \,\mathrm{and}$ -32, 32, 60, 80, 100, 200, 400, 800, 1000, $4000 \,\mathrm{mJy}$ beam $^{-1}$. Lower left-hand panel: the map of 3C 223.1 at 610 MHz matched with the resolution of 240 MHz. The contour levels are -10, 10,

example of a mirror symmetric distortion, but it is now described by rotational symmetry (Leahy & Williams 1984).

High-frequency spectral indices constructed at a resolution of $5.0 \times 4.8 \, \mathrm{arcsec^2}$ using images at $1.4, 1.7 \, \mathrm{and} \, 2.7 \, \mathrm{GHz}$ show indication for a spectral steepening towards the wings (Rottmann 2001). Author also finds a prominent spectral steepening from the south lobe to the west wing as compared to a mild spectral steepening from the north lobe to the east wing. Similar spectral steepening between $1.4 \, \mathrm{and} \, 5.0 \, \mathrm{GHz}$ from the south lobe to the east wing and from the north lobe to the west wing was also found by Alexander & Leahy (1987). The low-frequency fitted spectra have $-0.56 > \alpha > -1.24$ for all regions across the source. The source shows evidence for flatter spectra in the active lobes than in the wings. The east and west wings have spectral indices -1.24 ± 0.03 and -1.06 ± 0.02 , respectively, whereas the north and south active lobes have -0.56 ± 0.01 and -0.64 ± 0.01 , respectively.

(iv) $3C\ 136.1\ (z=0.064)$. It is a low galactic latitude object in the sample. An HST image of the host galaxy (Martel et al. 1999) shows flattened and warped host and bears no resemblance with an

elliptical galaxy. The host galaxy possibly has two/three nuclei and seems to be showing irregular, disrupted, possibly by tidal forces, signs of an ongoing merger.

Fig. 3 shows the radio images at 240- and 610-MHz; maps show similar extent and morphology along both axes, similar to its radio map at high frequency (Leahy & Williams 1984). Therefore, their suggestion that some of the large-scale structure may be missing from their map is unlikely. The core is clearly detected in 610-MHz maps and is marginally detected in 240-MHz maps.

The spectral index maps of 3C 136.1 using radio maps at 1.37, 4.85 and 10.45 GHz at resolutions of 69×69 and 147×147 arcsec² show a spectral gradient from the active lobes $(-0.50 > \alpha > -0.65)$ to the wings (Rottmann 2001). The spectral gradient is more pronounced along the east lobe $(\alpha = -0.6)$ to the south wing $(\alpha = -1.0)$ as compared to the spectral gradient along the west lobe $(\alpha = -0.7)$ to the north wing $(\alpha = -0.85)$. Alexander & Leahy (1987) also found a spectral steepening between 1.4 and 5.0 GHz from the west lobe to the core and from the east lobe to the north wing using the VLA and Cambridge 5-km Telescope. The low-frequency

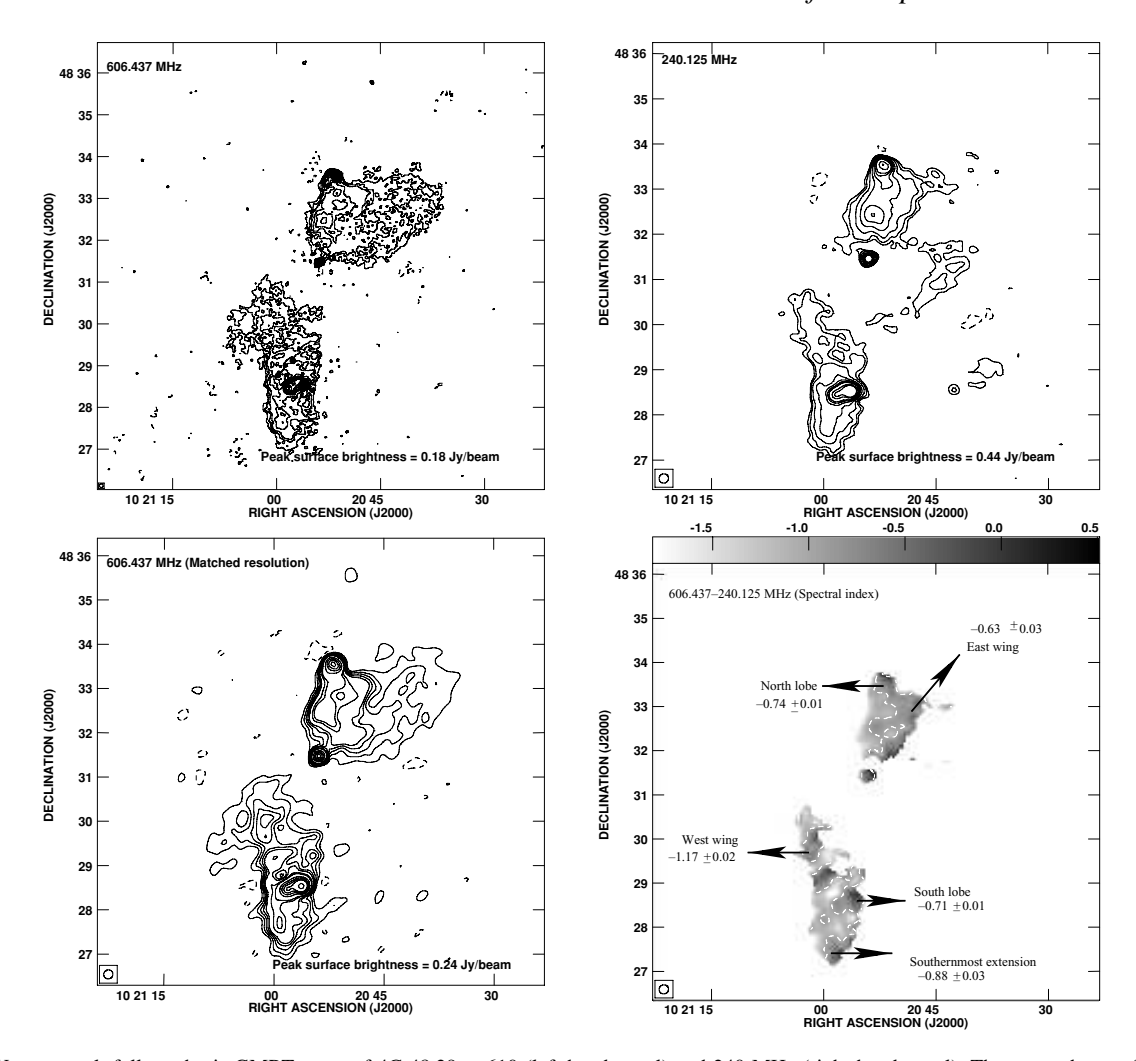


Figure 7. Upper panel: full synthesis GMRT maps of 4C 48.29 at 610 (left-hand panel) and 240 MHz (right-hand panel). The CLEAN beams for 610- and 240-MHz maps are 5.1×5.0 arcsec² at a PA of $-65^{\circ}.3$ and 12.6×12.2 arcsec² at a PA of $-48^{\circ}.9$, respectively, and the contour levels in the two maps are, respectively, -0.8, 0.8, 1, 2, 3, 4, 5, 6, 8, 10, 40 and -12, 12, 16, 24, 40, 60, 80, 100, 160, 200 mJy beam⁻¹. Lower left-hand panel: the map of 4C 48.29 at 610 MHz matched with the resolution of 240 MHz. The contour levels are -2, 2, 4, 6, 8, 10, 16, 20, 40, 60, 80, 100 mJy beam⁻¹. Lower right-hand panel: the distribution of the spectral indices, between 240 and 610 MHz, for the source. The spectral index contours are at -1, 0. The error bars in the full synthesis maps found at a source-free location are ~ 2.6 and ~ 0.2 mJy beam⁻¹ at 240 and 610 MHz, respectively.

fitted spectra have $-0.61 > \alpha > -0.76$ for all regions across the source. Similar to the high-frequency result, our result also shows evidence for steeper spectra in the wings than in the active lobes and the north and south wings have spectral indices -0.76 ± 0.03 and -0.71 ± 0.03 , respectively, whereas the east and west active lobes have -0.61 ± 0.14 and -0.61 ± 0.21 , respectively.

(v) $3C\ 192\ (z=0.060)$. 3C 192 was classified as an X-shaped source having prominent distorted structure of rotational type (Parma et al. 1985).

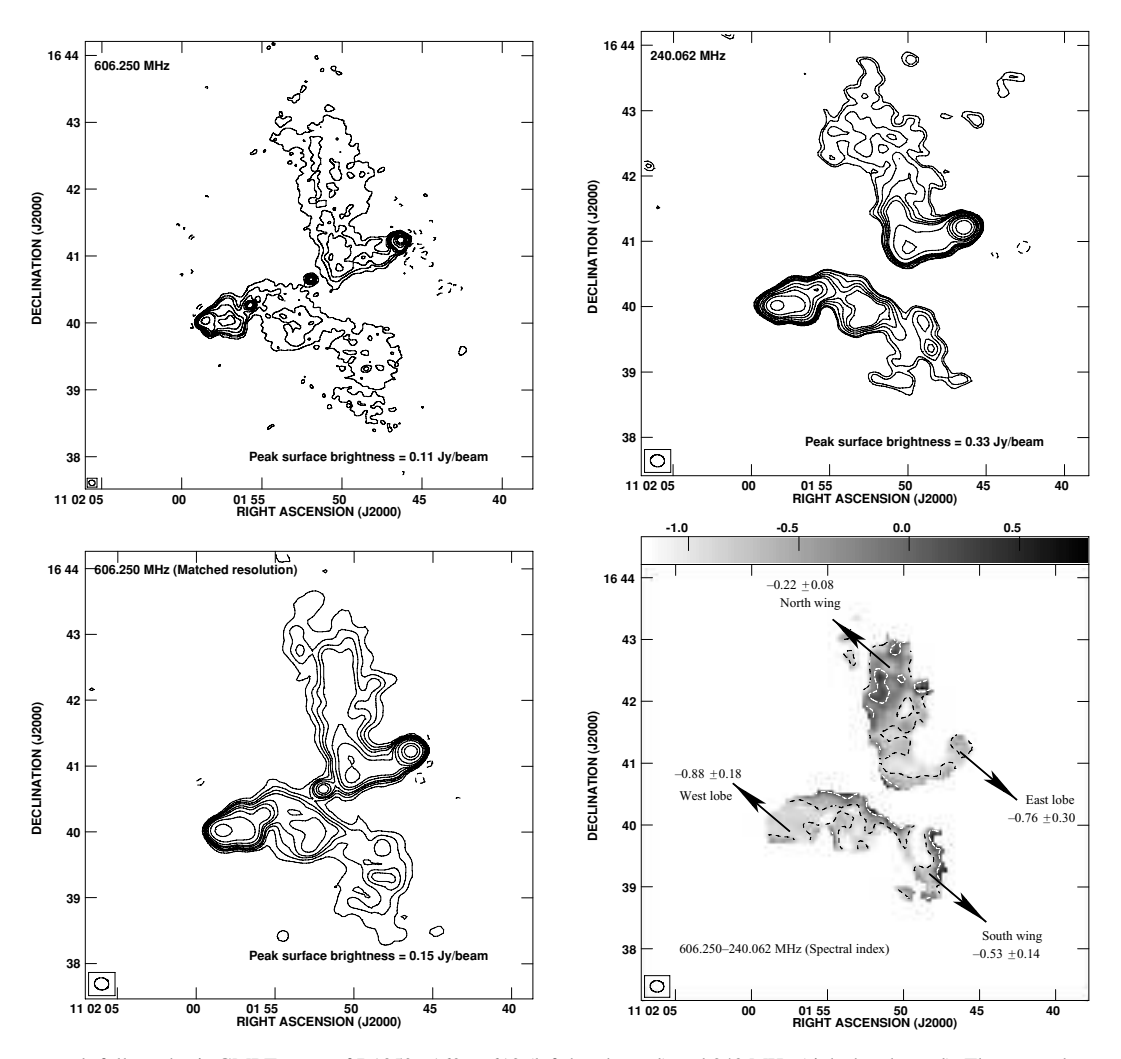
Fig. 4 shows the radio images at 240 and 610 MHz. The angular extents along the active axis and the wings are \sim 210 and \sim 120 arcsec, respectively, at both frequencies. Both the maps show similar radio extent along the active axis and along the wings, consistent with an earlier work (Högbom 1979; Dennett-Thorpe et al. 1999), and both the wings have symmetrical distortions. The radio structure in the central parts of this source is confused, but the detailed shape of the contours close to the position of the host galaxy clearly indicates the presence of a weak unresolved central compo-

nent. There is also a weak transverse feature across the south-east wing.

The low-frequency fitted spectra have $-0.82 > \alpha > -1.15$ for all regions across the source. The source shows evidence for comparable spectra in the active lobes than in the wings. The north-west and south-east wings have spectral indices -0.88 ± 0.03 and -0.98 ± 0.02 , respectively, whereas the north-east and south-west active lobes have -0.82 ± 0.01 and -1.15 ± 0.01 , respectively.

(vi) B20828 + 32(z = 0.053). B2 0828+32 is the most-extended X-shaped source in the sample. Although the host galaxy neither has a double core nor has a companion, the luminosity profile shows faint possibility of a merger event (Ulrich & Rönnback 1996).

Fig. 5 shows the radio images at 240 and 610 MHz. The source shows large scale 'S'-type distortions, suggestive of precession phenomenon of the central engine (Parma et al. 1985). The south-east-north-west axis consists of prominent hotspots, which is possibly the active axis, whereas the north-south axis is along the wings, which is barely visible in our maps and in our low-resolution $(30 \times 30\text{-}arcsec^2)$ maps. The faint detection of hotspot is likely



in our 610-MHz map and not in our low-resolution maps, which were earlier detected in high-resolution images at 1.4 and 5 GHz (Parma et al. 1985; Feretti et al. 1983). This is one of the first X-shaped source identified as two double radio structures of different ages and oriented at widely different angles (Ulrich & Rönnback 1996).

The high-frequency spectral index (1.4–10.55 GHz) exhibits a gradual steepening from the active lobes ($\alpha \simeq -0.7$) to the wings ($\alpha \simeq -1.1$, southern wing and $\alpha \simeq -1.1$, northern wing) (Rottmann 2001). The low-frequency fitted spectra have $-0.37 \geqslant \alpha \geqslant -2.79$ for all regions across the source. Even though the radio maps and the spectral index map are rather noisy, due mainly to the absence of the north wing and the south wing in our 240-MHz map, there is a weak evidence for steeper spectra in the active lobes than in the wings. The spectral index of the north wing is flatter than $\geqslant -2.79 \pm 0.30$ and of the south wing is steeper than $\leqslant -0.37 \pm 0.21$. Instead, the north-west and south-east active lobes have spectral indices of -1.27 ± 0.01 and -1.21 ± 0.01 , respectively.

(vii) 3C 223.1 (z = 0.108). The host galaxy was imaged as part of the *HST* snapshot survey (de Koff 1996) and the galaxy has a

strong central bulge and a very pronounced dust disc. The source is believed to be isolated or in a poor group (Sandage 1972) and no X-ray emission was detected from it or at its surroundings (Burns, Gregory & Holman 1981).

Fig. 6 shows complex radio source with an X-shaped morphology at both 240 and 610 MHz. The angular extent is $\sim \! 105$ arcsec along the active lobes (those with hotspots) and $\sim \! 150$ arcsec along the wings. The nuclear source of 3C 223.1 is invisible at both these frequencies and also in the radio maps of Dennett-Thorpe et al. (2002), but is detected and is unresolved at 8.4 GHz (Black et al. 1992). The weak jet detected mid-way between the core and north lobe at 8.4 GHz (Black et al. 1992) is not seen in our maps because of coarser resolution. Our maps also suggest a sharp boundary at the farthest end of the north lobe and a likely ring-like feature in the south lobe, which is consistent with earlier results.

The low-frequency fitted spectra have $-0.37 > \alpha > -1.08$ for all regions across the source, and is the first X-shaped source showing evidence for steeper spectra in the active lobes than in the wings (Lal & Rao 2005). Here, we do look into the errors that would be introduced due to possible negative depression. The maximum

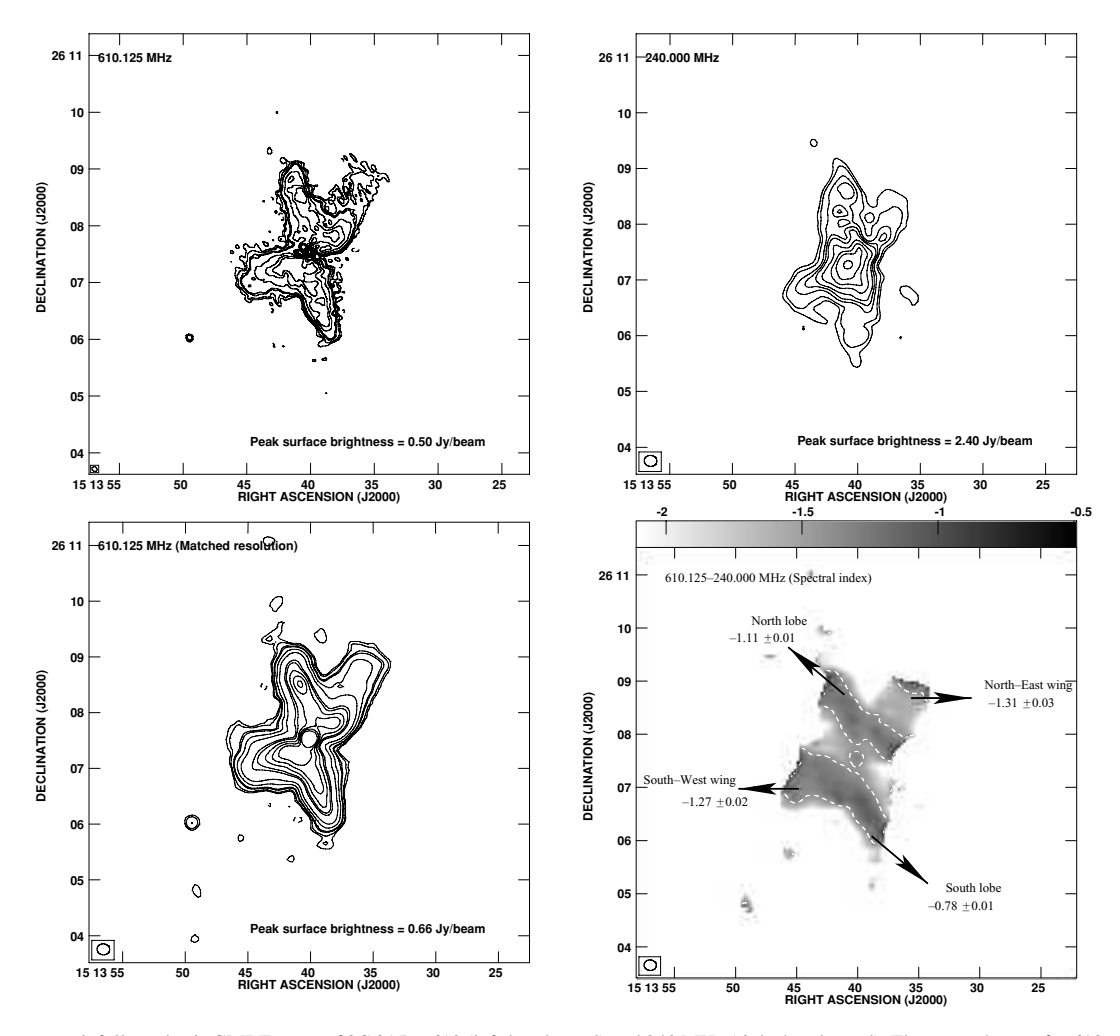


Figure 9. Upper panel: full synthesis GMRT maps of 3C 315 at 610 (left-hand panel) and 240 MHz (right-hand panel). The CLEAN beams for 610- and 240-MHz maps are $5.7 \times 4.7 \, \mathrm{arcsec^2}$ at a PA of 62° .0 and $13.6 \times 11.8 \, \mathrm{arcsec^2}$ at a PA of 84° .1, respectively, and the contour levels in the two maps are, respectively, -2, 2, 4, 8, 20, 30, 40, 80, 100, 200, 400, 800 and -160, 160, 240, 400, 500, 600, 800, 1000, 1200, 2000 mJy beam $^{-1}$. Lower left-hand panel: the map of 3C 315 at 610 MHz matched with the resolution of 240 MHz. The contour levels are -3, 3, 4, 8, 10, 20, 40, 100, 120, 160, 200, 240, 300 mJy beam $^{-1}$. Lower right-hand panel: the distribution of the spectral indices, between 240 and 610 MHz, for the source. The spectral index contours are at -1.7, 0.5. The error bars in the full synthesis maps found at a source-free location are ~ 6.8 and ~ 0.3 mJy beam $^{-1}$ at 240 and 610 MHz, respectively.

depression close to the source at 240 and 610 MHz is -7.6 and -2.7 mJy beam $^{-1}$, respectively. This worst case would introduce a maximum error of 0.14 in spectral indices for the wings and 0.01 for the active lobes. The east and west wings have spectral indices -0.37 ± 0.14 and -0.62 ± 0.14 , respectively, whereas the north and south active lobes have -1.08 ± 0.01 and -1.08 ± 0.01 , respectively, and are consistent with spectral results between 1.4 and 32 GHz, that is, -0.70 ± 0.03 and -0.66 ± 0.03 for the east and west wings, and -0.75 ± 0.02 and -0.77 ± 0.02 for the north and south active lobes, respectively (Dennett-Thorpe et al. 2002). Since the observed differences in spectral index at low frequencies are much more than the uncertainties, we believe that the observed spectral index features are real. Similar result, 'spectral reversal', was also found independently by Rottmann (2001).

(viii) 4C 48.29 (z=0.053). This source is the nearest to us and is at the centre of Abell 990 cluster. The parent galaxy belongs to a double system with no visible companion on the Palomar Sky Survey (PSS) prints (Parma et al. 1985), but a companion is detected, \sim 25 arcsec away on the south-east on the Two-Micron All-Sky Survey (2MASS), which is probably a starburst galaxy.

Fig. 7 shows the radio images at 240 and 610 MHz and they show that the brightest components of the hotspots are well aligned with the core, which is consistent with the results of van Breugel & Jägers (1982). The source has a peculiar X-shaped morphology with an additional wing-like feature at the south of the south active lobe. Furthermore, 240-MHz map shows a low surface brightness feature \sim 2 arcmin to the east and a point source \sim 4 arcmin to the south-east of the core.

The low-frequency fitted spectra have $-0.63 > \alpha > -1.17$ for all regions across the source. The east and west wings have spectral indices -0.63 ± 0.03 and -1.17 ± 0.02 , respectively, whereas the north and south active lobes have -0.74 ± 0.01 and -0.71 ± 0.01 , respectively. Furthermore, the southernmost extension has a spectral index of -0.88 ± 0.03 . Briefly, the east wing definitely shows evidence for flatter spectra than either of the two active lobes; otherwise, the rest of the regions have comparable spectral indices.

(ix) B1059+169 (z=0.068). B1059+169 is the another source seen in cluster environment (Abell 1145), which is the dominant radio galaxy and is \sim 5.5 arcmin away from the cluster centre. A

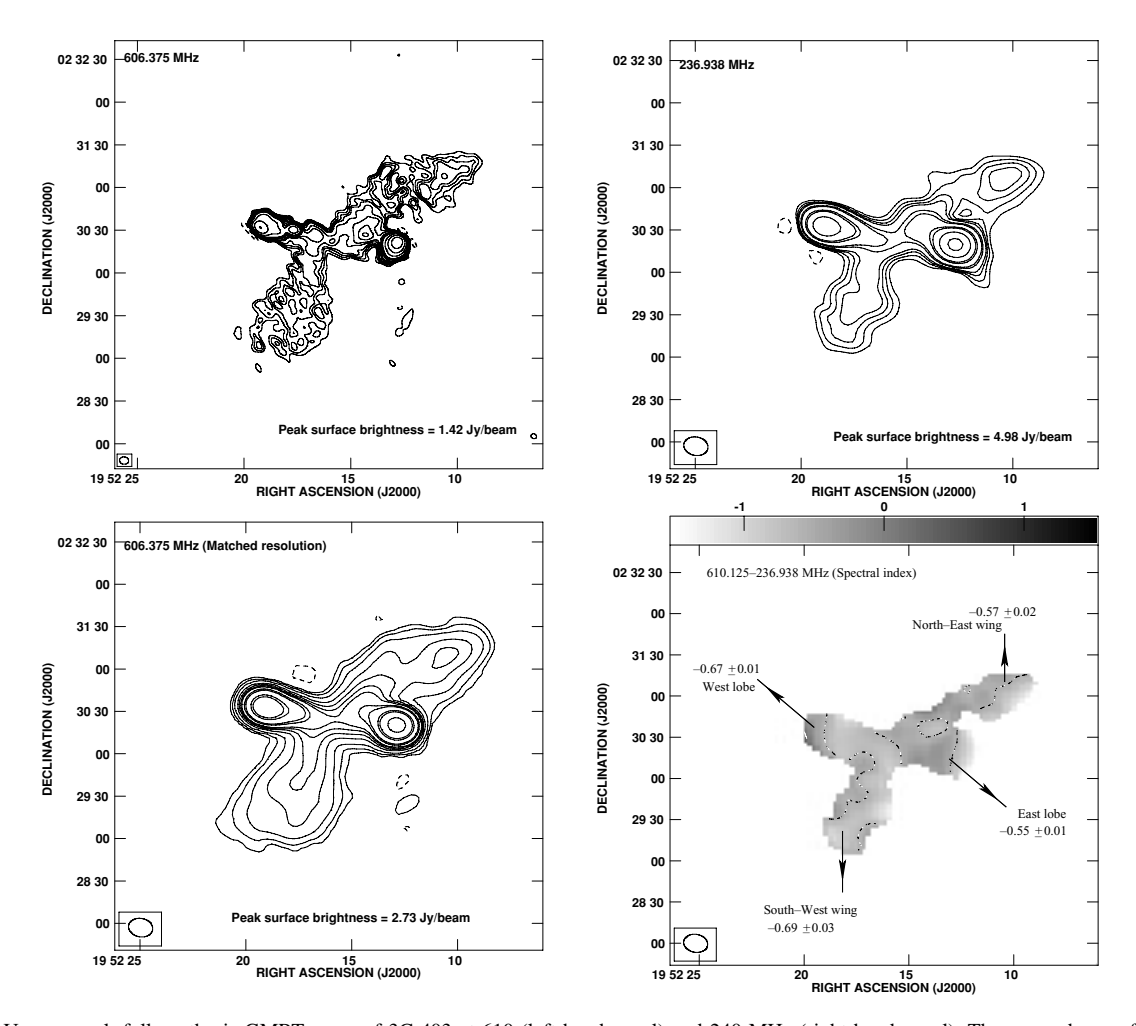


Figure 10. Upper panel: full synthesis GMRT maps of 3C 403 at 610 (left-hand panel) and 240 MHz (right-hand panel). The CLEAN beams for 610- and 240-MHz maps are $6.4 \times 5.1 \,\mathrm{arcsec^2}$ at a PA of 85° .3 and $17.3 \times 13.1 \,\mathrm{arcsec^2}$ at a PA of 79° .0, respectively, and the contour levels in the two maps are, respectively, -8, 8, 12, 16, 20, 30, 40, 60, 80, 100, 200, 400, 800 and -80, 80, 120, 160, 200, 320, 400 800 1000 mJy beam $^{-1}$. Lower left-hand panel: the map of 3C 403 at 610 MHz matched with the resolution of 240 MHz. The contour levels are -10, 10, 20, 40, 80, 120, 160, 200, 320, 400, 800, 1000 mJy beam $^{-1}$. Lower right-hand panel: the distribution of the spectral indices, between 240 and 610 MHz, for the source. The spectral index contours are at -0.6, 0.2. The error bars in the full synthesis maps found at a source-free location are \sim 4.8 and \sim 0.5 mJy beam $^{-1}$ at 240 and 610 MHz, respectively.

companion is detected on the 2MASS, coincident with the cluster centre.

The morphology at low frequency (Fig. 8) is similar to the 1.4-GHz map of Owen & Ledlow (1997). The extent of the east—west active axis is 200 arcmin in both the maps, whereas the extent of the north—south axis in the 240-MHz map is 310 arcmin, which is slightly more than the extent of the wings in the 610-MHz map. This could be possibly due to spectral ageing, which is a common phenomenon for head—tail and wide-angle-tail radio sources, seen in clusters, exhibiting low surface brightness features. In the 610-MHz map, we also detect a knot in between the west lobe and the core.

The low-frequency fitted spectra have $-0.22 > \alpha > -0.88$ for all regions across the source. Although B1059+169 is found in the cluster environment, surprisingly, the spectral results of it are similar to that of 4C 12.03 and 3C 223.1, that is, the wings have relatively flatter spectral index as compared to the active lobes. The north and south wings have spectral indices -0.22 ± 0.08 and -0.53 ± 0.14 , respectively, whereas the east and west active lobes have -0.76 ± 0.30 and -0.88 ± 0.18 , respectively. Furthermore, the knot

in between the west lobe and the core has a spectral index of -0.82 ± 0.22 , similar to the east and west active lobes.

(x) 3C 315 (z = 0.108). Similar to NGC 326 and 4C 48.29, here also, the host galaxy belongs to a double system with no visible companion on the PSS prints (Parma et al. 1985), but ~7 arcsec away on the south, a companion is detected on the 2MASS, and is identified to be a irregular galaxy. Their optical profiles show signs of interaction and seem to be located in a poor cluster (Zirbel 1997). An *HST* image of the northern core containing the radio source shows an elliptical host (de Koff 1996).

Fig. 9 shows the radio images at 240 and 610 MHz with both the axes to be roughly of similar angular sizes and surface brightnesses, making it a very unusual source (Alexander & Leahy 1987). However, as suggested by Högbom (1979), the jet along the north—south axis being of slightly higher surface brightness and could define a recent axis of activity. The core is clearly detected in both the radio maps and is associated with the brightest member of a pair of elliptical galaxy (Leahy & Williams 1984). Furthermore, the source does not display characteristic elongated structure, that is, the usual hotspots at or near the extreme edges.

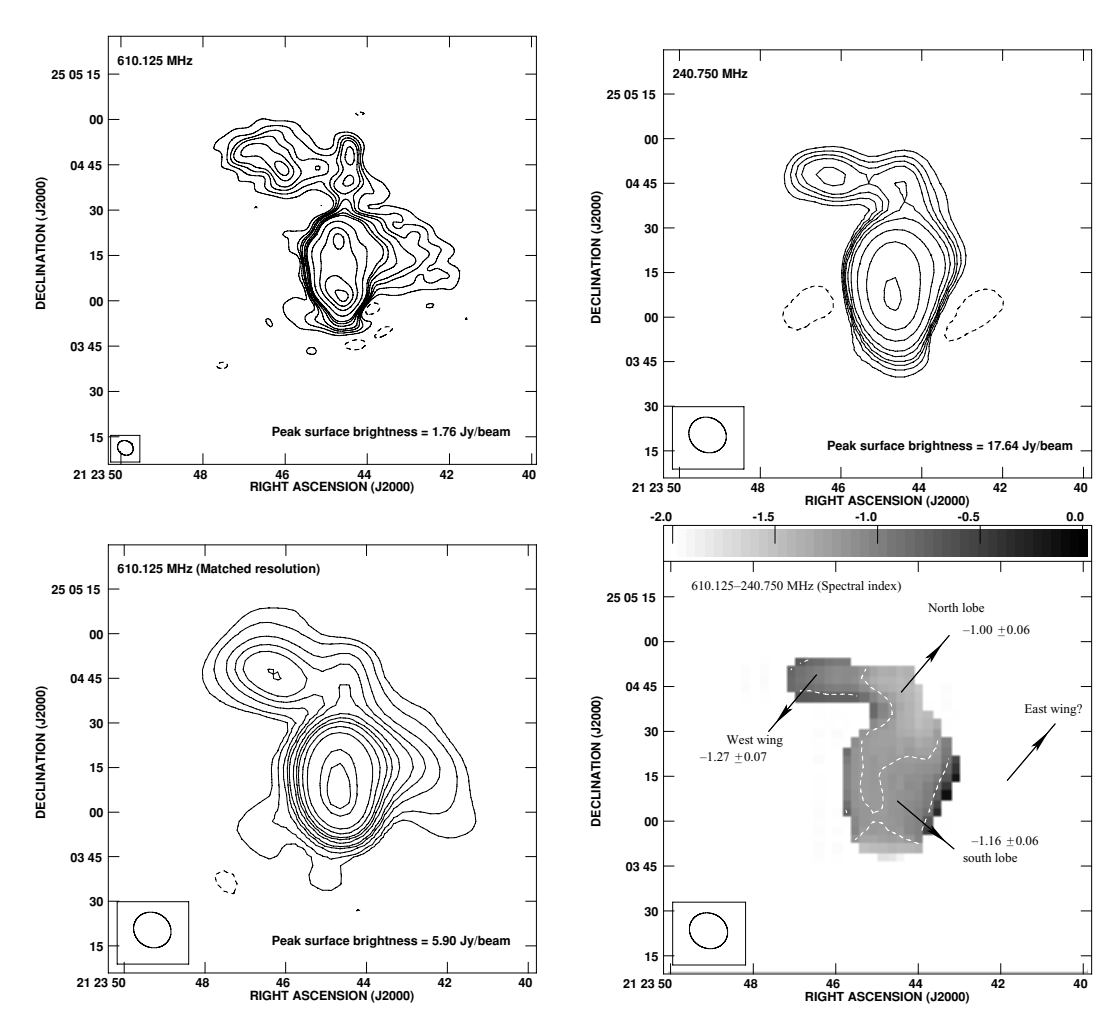


Figure 11. Upper panel: full synthesis GMRT maps of 3C 433 at 610 (left-hand panel) and 240 MHz (right-hand panel). The CLEAN beams for 610- and 240-MHz maps are $5.4 \times 4.6 \,\mathrm{arcsec^2}$ at a PA of 57° .0 and $12.9 \times 11.6 \,\mathrm{arcsec^2}$ at a PA of 58° .7, respectively, and the contour levels in the two maps are, respectively, -20, 20, 40, 60, 80, 120, 160, 200, 400, 800, 1200 and -400, 400, 600, 800, 1000, 1400, 2000, 4000, 8000 mJy beam⁻¹. Lower left-hand panel: the map of 3C 433 at 610 MHz matched with the resolution of 240 MHz. The contour levels are -50, 50, 100, 200, 300, 400, 600, 800, 1000, 1400, 2000, 4000 mJy beam⁻¹. Lower right-hand panel: the distribution of the spectral indices, between 240 and 610 MHz, for the source. The spectral index contours are at -1.2, -0.8, 0. The error bars in the full synthesis maps found at a source-free location are \sim 6.9 and \sim 0.8 mJy beam⁻¹ at 240 and 610 MHz, respectively.

Table 2. The total intensity for all the sources. The total flux densities quoted are in Jy along with corresponding error bars (1σ) . The 240 and 610 MHz are our GMRT measurements.

	178 MHz	240 MHz	408 MHz	610 MHz	1400 MHz	2695 MHz	4850 MHz
4C 12.03	7.6 ± 1.0^{a}	6.62 ± 0.12	4.45 ± 0.20^{b}	2.94 ± 0.05	2.01 ± 0.10^{c}		0.54 ± 0.07^d
3C 52	13.7 ± 1.1^{a}	11.71 ± 0.68		6.44 ± 0.40	3.80 ± 0.19^{e}	2.30 ± 0.12^{e}	1.55 ± 0.17^d
3C 136.1	14.0 ± 2.1^{e}	10.41 ± 0.05		5.76 ± 0.03	2.90 ± 0.44^{e}	2.08 ± 0.10^{e}	0.56 ± 0.75^d
3C 192	21.0 ± 3.2^{e}	20.51 ± 0.28	11.03 ± 0.90^f	9.08 ± 0.12	4.80 ± 0.20^{f}	3.23 ± 0.16^f	2.68 ± 0.10^{f}
B2 0828+32		7.17 ± 0.05		2.23 ± 0.02	$2.07 \pm 0.10^{\circ}$		0.44 ± 0.06^d
3C 223.1	8.7 ± 1.1^{g}	8.33 ± 0.41	4.72 ± 0.10^{h}	3.56 ± 0.17	1.90 ± 0.28^{i}	1.23 ± 0.61^{e}	0.78 ± 0.11^{j}
4C 48.29	4.5 ± 0.6^{a}	5.73 ± 0.04		2.56 ± 0.03			0.35 ± 0.04^d
B1059+169		1.61 ± 0.02	1.02 ± 0.22^{b}	0.80 ± 0.01	$0.62 \pm 0.10^{\circ}$		0.21 ± 0.03^d
3C 315	20.3 ± 1.7^{f}	39.83 ± 0.33	10.62 ± 0.87^f	8.95 ± 0.09	4.10 ± 0.20^f	2.39 ± 0.05^f	1.28 ± 0.17^d
3C 403	30.9 ± 4.0^{f}	17.62 ± 0.72	13.57 ± 0.59^b	9.81 ± 0.38	6.05 ± 0.19^f	3.65 ± 0.18^f	2.06 ± 0.10^{f}
3C 433	60.4 ± 4.8^{f}	57.75 ± 3.98	29.26 ± 2.30^f	20.59 ± 1.21	12.40 ± 0.35^f	6.63 ± 0.33^f	4.05 ± 0.54^d

^aLarge Cambridge Interferometer (Ryle 1960; Gower, Scott & Wills 1967). ^bThe Molonglo reference catalogue of radio sources (Large et al. 1981). ^cGreen Bank, Northern Sky Survey (White & Becker 1992). ^dGregory & Condon (1991). ^eKellermann Pauliny-Toth & Williams (1969). ^fKuhr et al. (1981). ^gLarge Cambridge Interferometer (Pilkington & Scott 1965). ^hFicarra, Grueff & Tomassetti (1985). ^fVLA FIRST survey (Becker et al. 1995). ^fGreen Bank, Northern Sky Survey (Becker, White & Edwards 1991; White & Becker 1992).

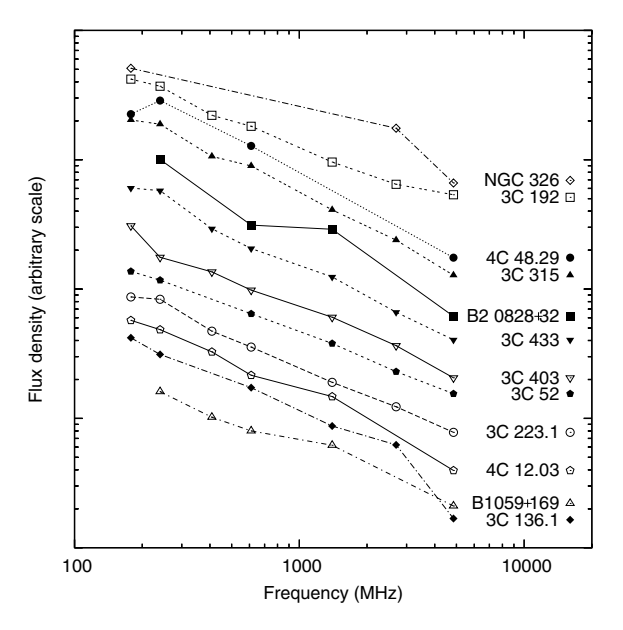


Figure 12. Integrated flux density (spectra) for the sample of X-shaped sources. Various measurements along with the error bars (not plotted) are explained in Table 2. The spectra are shifted with respect to one another for clarity.

The spectral index map of 3C 315 using the radio maps at 1.65 and 2.7 GHz at a resolution of $9.1 \times 5.5 \,\mathrm{arcsec^2}$ shows relatively flat spectral index regions close to the core and steep spectral index regions being located at the tips of the active lobes. The southern and northern active lobes have high-frequency (1.65–2.7 GHz) spectral indices, -1.46 and -1.26, respectively (Rottmann 2001). The low-frequency fitted spectra have $-0.78 > \alpha > -1.31$ for all regions across the source, and show evidence for flatter spectra in the active lobes than in the wings. The north-east and south-west wings have spectral indices -1.31 ± 0.03 and -1.27 ± 0.02 , respectively, whereas the north and south active lobes have -1.11 ± 0.01 and -0.78 ± 0.01 , respectively. The spectral index map (Fig. 9, lower right-hand panel) shows peculiar spectral behaviour and is consistent with the findings of Alexander & Leahy (1987) and Rottmann (2001), that is, the spectrum is steep at the wings, it becomes flatter in regions close to the core, and again steepens towards the active lobe and ultimately becomes steepest at the tip of the active lobes.

(xi) $3C\ 403\ (z=0.059)$. The host of 3C 403 is a E0, narrow-line radio galaxy (NASA/IPAC Extragalactic Database classification) and the continuum colours are typical of an early-type galaxy. The galaxy appears to be a smooth elliptical using the *HST* with an apparent separation of the source into a central elliptical region and a low surface brightness halo, which is probably due to intervening dust (Martel et al. 1999). The host galaxy does not have any bright companion and is located in a very low density local galaxy environment (Heckman et al. 1994).

Fig. 10 shows the radio images at 240 and 610 MHz, and the east and west hotspots are clearly detected. The slightly larger angular extent of the north–south axis along the wings in the 240-MHz map than in the 610-MHz and high-frequency maps (Dennett-Thorpe et al. 1999) could be due to spectral ageing.

The low-frequency fitted spectra have $-0.55 > \alpha > -0.69$ for all regions across the source. The south-west and north-east wings have spectral indices -0.69 ± 0.03 and -0.57 ± 0.02 , respectively,

Table 3. Flux densities of all the distinct regions at 240 and 610 MHz. The error bars for these sources are quoted in the respective figure captions.

		Flux density 240 MHz	610 MHz
		(mJ	y)
4C 12.03	North lobe	2214.9	915.0
	South lobe	1376.3	618.9
	East wing	117.5	67.8
	West wing	91.5	47.6
3C 52	North lobe	5312.0	3035.9
	South lobe	2395.0	1314.4
	East wing	384.0	121.2
	West wing	272.6	101.8
3C 136.1	East lobe	904.0	511.3
	West lobe	2149.0	1214.6
	North wing	163.5	80.2
	South wing	159.5	82.4
3C 192	North-east lobe	383.2	167.9
	South-west lobe	478.7	192.0
	South-east wing	2351.3	1091.5
	North-west wing	2405.8	824.8
B2 0828+32	South-east lobe	1288.8	416.8
	North-west lobe	1213.4	372.0
	North wing	<13.5 ^a	$< 1.0^{a}$
	South wing	<13.5 ^a	19.1
3C 223.1	North lobe	2946.1	1074.9
	South lobe	3268.6	1196.7
	East wing	123.8	87.8
	West wing	175.5	98.3
4C 48.29	North lobe	462.2	232.3
	South lobe	689.7	356.8
	East wing	51.9	28.9
	West wing	98.9	33.2
	Southernmost	251.5	110.4
B1059+169	East lobe	210.3	92.4
	West lobe	226.7	111.6
	North wing	25.9	21.0
	South wing	23.5	14.4
3C 315	North lobe	1140.6	403.6
	South lobe	938.2	453.7
	North-east wing	1018.3	300.6
	South-west wing	977.5	291.7
3C 403	East lobe	5856.9	3133.0
	West lobe	3740.9	2241.7
	North wing	512.1	300.1
	South wing	549.5	287.9
3C 433	North lobe	1685.3	663.5
	South lobe	21 025.0	7066.3
	East wing	$< 34.0^{a}$	831.1
	West wing	1530.8	467.0

^aThe upper limits on the flux densities quoted are five times the rms noise levels

whereas the east and west active lobes have -0.55 ± 0.01 and -0.67 ± 0.01 , respectively. These results are inconsistent with results at high frequency (Rottmann 2001; Dennett-Thorpe et al. 2002), that is, the spectral indices between 1.4 and 32 GHz are -0.80 ± 0.03 and -0.77 ± 0.28 for the south-west and north-east wings, respectively (note that Dennett-Thorpe et al. 2002 labelled the south-west and north-east wings as the south-east and north-west wings, respectively), and -0.78 ± 0.02 and -0.77 ± 0.02 for the east and west active lobes, respectively. Instead, the source shows evidence for comparable spectra in the active lobes and the wings.

(xii) 3C 433 (z = 0.102). The host has a disturbed morphology (PSS prints) with no known nearby companion and lies in a cluster (McCarthy, Spinard & van Breugel 1995). An HST image of the source shows a galaxy full of filaments of dust, a faint patch of emission north-west of the galaxy coinciding with a spot of radio emission and possible regions of star formation (de Koff 1996).

Fig. 11 shows the radio images at 240 and 610 MHz. Since our map at 240 MHz is a low-resolution map, therefore, several features seen in van Breugel et al. (1983) and Black et al. (1992) are smoothed, and it is unclear if the source is indeed an X-shaped source. Instead, the 610-MHz map shows many of the features to be clearly resolved similar to the VLA map at 6 cm (van Breugel et al. 1983; Black et al. 1992). We clearly detect weak, collimated emission to the north from the lobe forming A, B and C (for the positions of A-I, see Fig. 1(a) of van Breugel et al. 1983). The eastern feature, D, is also clearly detected. As suggested by van Breugel et al. (1983), the south lobe seems to flare out close to the nucleus with a relatively large opening angle forming the eastern jet along I. We define regions centred at B and H to be the north and south active lobes, respectively, and we believe that the two lobes do not appear to be relaxed systems. The low surface brightness regions centred at D and I are, respectively, assumed to be the east and west wings for our further analysis.

We do not detect the east wing in our low-frequency map and the fitted spectra have $-1.00 > \alpha \geqslant -3.42$ for all regions across the source. The source shows marginal evidence for comparable spectra in the active lobes and the wings. The west wing has spectral index -1.27 ± 0.03 and the east wing is flatter than $\geqslant -3.42 \pm 0.21$, whereas the north and south active lobes have -1.00 ± 0.03 and -1.16 ± 0.01 , respectively. Here again we quantify the errors introduced due to possible negative depression, being -94.2 and -10.1 mJy beam⁻¹ at 240 and 610 MHz, respectively, close to the source, thereby introducing a maximum error of 0.07 in spectral indices for the wings and 0.06 for the active lobes, which are smaller than the quoted statistical errors.

6 DISCUSSION

The low-frequency GMRT observations combined with observations at other wavelengths raise a number of questions regarding the nature and the formation scenario of the X-shaped sources. Some of the earlier scenarios that were based on limited information need to be investigated. In this section, we first discuss the overall source morphological and spectral properties (Section 6.1). We then weigh all the *pros and cons* of existing models (Section 6.2), and statistical implications of these results on our understanding of the current formation models for the known sample of X-shaped sources (Section 6.3). Finally, in Section 6.4, we address the question, do X-shaped sources constitute a single class in light of 'merger of two AGNs' model.

6.1 Overall source properties

Nearly a dozen sources have been mapped in detail with a resolution approaching to \sim 1 kpc in most cases. Here, a few qualitative points about the overall source morphological and spectral properties, based on images presented, are made.

6.1.1 Source morphological properties

The salient features of morphology of all X-shaped sources are as follows.

- (i) Almost all sources show similar angular sizes for the two axes. Marginal differences between two axes in 3C 192 and 3C 403 can be attributed to the projection effects.
- (ii) Source 3C 315 has all four lobes of almost similar surface brightness, thereby making it difficult to identify the active lobes and the wings.
- (iii) Although 3C 433 is classified as an X-shaped source, it does not have 'typical' 'X'-shape morphology. It is also the source with smallest angular size in the sample.
- (iv) The radio core is detected for only one of the source, B1059+169, in its 610-MHz map, whereas the radio maps of sources 4C 12.03, 4C 48.29 and 3C 315 at 610 MHz show marginal detection of the radio cores.
- (v) Hotspots are almost always detected in the high surface brightness active lobes in both 610- and 240-MHz radio maps.
- (vi) We detect the high surface brightness jets in almost, in fact, all the X-shaped sources, and this nearly 100 per cent high rate of jet detection is similar to that of Leahy et al. (1997) and Hardcastle et al. (1997) for classical radio sources.

6.1.2 Global spectral morphological properties

The integrated radio flux densities at several locations across each of these sources allow us to group them into the following three categories. (i) Sources in which the wings are of flatter spectral indices than that of the active lobes, that is, 4C 12.03, 3C 223.1 and B1059+169. These sources have spectral indices $-0.22 > \alpha_{\text{wings}} >$ -0.70 and $-0.76 > \alpha_{active lobes} > -1.08$ for all regions across the source. In addition, in the former two sources, the wings (or low surface brightness jets) have flatter spectral indices with respect to the high surface brightness jets at high radio frequencies (Rottmann 2001; Dennett-Thorpe et al. 2002), consistent with our low-frequency results. (ii) Sources in which the wings and the active lobes have comparable spectral indices, that is, 3C 192, B2 0828+32, 4C 48.29 and 3C 403. Here, these classes of sources have spectral indices $-0.37 \geqslant \alpha_{wings} \geqslant -2.79$ and -0.55 > $\alpha_{active \, lobes} > -1.27$ for all regions across the source. It therefore seems that although the two regions, the wings and the active lobes, have comparable spectral indices, they are relatively flat as compared to typical steep spectrum features. It is important to note that, since we have limits for spectral indices of the north and south wings, we have included B2 0828+32 in this category, although the south wing seems to be flatter than the active lobes. (iii) Sources in which the wings are of steeper spectral indices as compared to the active lobes, that is, NGC 326, 3C 52, 3C 136.1, 3C 315 and 3C 433. This category of sources have spectral indices -0.71 > $\alpha_{wings} \geqslant -3.42$ and $-0.56 > \alpha_{active \, lobes} > -1.16$ for all regions across the source. This latter class of sources are similar to typical radio galaxies, where low surface brightness features have steeper spectral indices as compared to the high surface brightness features, which have relatively flat spectral indices. The results of the former two classes of sources are unusual, and we believe that it is not due to possible artefacts, for example, different UV coverages, images containing negative depression around the source, image misalignment at 240 and 610 MHz, etc. Also, these results do not support the known formation scenarios, discussed below, in which the wings are interpreted as relics of past radio jets and the active lobes as the newer ones.

Furthermore, the results from this class of sources are consistent with earlier results that there is no trend of spectral index with jet side at any brightness level, which has been a subject of considerable

debate (Black et al. 1992; Dennett-Thorpe et al. 1999; Dennett-Thorpe et al. 2002).

6.2 Formation models

The most intriguing fact about X-shaped radio galaxies is the apparently small number of sources of X-shape. Two possible explanations for the small number are (i) they are very exotic objects that form only rarely and under extraordinary circumstances, and (ii) they are normal radio galaxies that are currently in a short-lived and/or rare phase of their evolution (Rottmann 2001). In order to explain these, it is necessary to understand the formation process responsible for the X-shaped phenomenon. We briefly introduce the key formation mechanisms and discuss them in light of existing observational results.

6.2.1 Backflow

Leahy & Williams (1984) have argued in favour of backflow being responsible for the formation of the wings of X-shaped sources. Backflow is formed by jet material that is released by the hotspots and is then streaming back towards the host galaxy. In the model, the backflow material remains collimated until it meets the backflow from the opposite hotspot and expands laterally into a fat disc oriented perpendicular to the radio lobe axis. For physical conditions prevailing in the lobes of radio galaxies, with typical advance speed of the hotspots of a few per cent of c, high apparent backflow speeds have been inferred with roughly a constant ratio of the speed of advance to the speed of backflow (Scheuer 1995). Assuming backflow velocities close to magnetosonic sound speed, though real flows occur at lower speeds, and typical secondary lobe lengths of a few hundred kpc, one requires a duration of the order of a few 10⁷ yr for matter to flow from the core to the tips of the secondary lobes. This is less than the radiative age, $\sim 10^8$ yr, of X-shaped sources assuming an equipartition of energy between the radiating particles and magnetic field and 610 MHz as the break frequency of the injected electron population, and/or the typical radio source lifetime of 10⁸ yr (Rottmann 2001). Furthermore, this being an optimistic estimate, the true lobe lengths are larger if projection effects are taken into account, which would increase the required flow speeds. On top, once the backflowing material leaves the primary lobes and has to penetrate into the ambient medium, we expect the flow to be decelerated by ram-pressure. Therefore, the required flow duration will thus be closer to a few 10⁸ yr, which would make backflow unlikely as the dominant formation scenario unless X-shaped sources prove to be unusually old.

6.2.2 Buoyancy

On morphological grounds, the lobes of a radio galaxy have a lower density than the surrounding medium (Williams 1991). Therefore, it is expected that buoyancy may have an impact on the large-scale morphology of the radio lobes. Worrall et al. (1995) have applied such a buoyancy model to NGC 326 and is unable to account for the formation of X-shaped radio galaxies. X-ray studies of gaseous environment of several such sources were not able to detect significant cluster gas emission (Kraft et al. 2005) with the exception of NGC 326. Although this might be due to lack of sensitivity, the buoyancy model is also faced with the problem of rotational symmetry of X-shaped radio galaxies. The two angles between the primary and secondary lobes of an X-shaped source are typically equal to within $\pm 10^\circ$, and if buoyancy would be a dominant formation process one would expect to find a more random distribution of these

angles (Rottmann 2001). Also, the radio source must do significant work on the medium, and the total work must be comparable to the stored energy within the lobes (Kaiser & Alexander 1997, 1999). Typically, the time-scale for formation of such sources or the corresponding radius out to which the source expanded is the age of the source times the average Mach number (<1) for expansion (Alexander 2002), which is an order of magnitude less than the age of the source. In addition, the swept-up gas would become Rayleigh–Taylor unstable, since the density of the cocoon is very much less than the external swept-up material (Scheuer 1974).

Therefore, we also conclude that buoyancy will influence the large-scale structure of radio galaxies only in dense cluster environments as is seen for wide-angle-tail radio sources in cluster of galaxies, and it is implausible that buoyancy, without a favourable configuration of the interstellar medium or intergalactic medium, would influence the structure of X-shaped sources.

6.2.3 Conical precision

The conical precession model (Parma et al. 1985; Mack et al. 1994) requires not only a fortuitous angle between the precession cone and angle to the line of sight, but also a happy accident of the positions at which the source first switched on and its position now. It therefore seems unlikely that we can explain the number of such sources seen, or the lack of other related sources (Leahy & Parma 1992).

More importantly, the morphologies of these sources do not seem to fit conical precision model (Dennett-Thorpe et al. 2002). Structures linking the wing and the lobe should at least be detected at low radio frequencies, if the morphology arose from a special projection of a slowly precessing source. Instead, in almost all the sources, there is a notable lack of such a feature. Furthermore, the wings being embedded well into the base also argues against any interpretation in terms of slow motion of the jet axis. Given these arguments, it is unimaginable that such precession can be used as an explanation for X-shaped sources.

6.2.4 Reorientation of the jet axis

Although at this point we conclude that the most likely formation process of X-shaped radio galaxies is reorientation of their jet axis due to a minor merger, an apparent contradiction of the model is posed by the small number of X-shaped radio galaxies as compared to the rather large number of minor merger events. The typical duration of the AGN phase is $\sim\!10^7$ yr. Since time-scale for jet reorientation is short, $\lesssim\!10^7$ yr (Dennett-Thorpe et al. 2002), or it occurs instantaneously (Merritt & Ekers 2002), Merritt & Ekers (2002) predicted both types of sources, X-shaped galaxy and radio galaxy, to be visible for a similar time. In other words, similar number of sources for both types are expected.

Certainly, selection effects due to projection and beaming can conceal the X-shaped nature of some sources on unfavourable viewing angles. For moderate intrinsic angles, the fraction of sources hidden by selection effects is ~25 per cent (Rottmann 2001). This suggests that, unless there is a large, hidden population of objects with very small reorientation angles, selection effects are not significant and insufficient to account for small number of X-shaped sources. Another problem for the connection of merging and reorientation arises when inspecting the environments in which the hosts of X-shaped sources are embedded. None of the known sources lay in dense clusters; only a few sources seem to be located in small, poor clusters or groups and the rest of the sources seem to be isolated field galaxies. Although the latter problem could be reconciled in

a minor merger model, leading to a sudden flip in the direction of any associated jet (Merritt 2004), we still need to address the small number of X-shaped radio galaxies as compared to the rather large number of minor merger events.

6.3 Implications on the formation models

We now discuss the implications on the assumptions of the spectral ageing method and discuss what could be the realistic formation model of X-shaped sources.

6.3.1 The assumptions of the spectral ageing method

It is possible that the assumptions used in the spectral ageing method for estimating the age need to be investigated. Due to the presence of all categories of sources, (i), (ii) and (iii), one of the assumptions, the low surface brightness wings are in the process of becoming new active jets, mentioned earlier (Lal & Rao 2005) does not seem true. Furthermore, presence of exotic re-acceleration mechanism is unlikely because of absence of any shock signatures. Also, the high degree of polarized emission observed in the wings (Rottmann 2001) indicates that the stochastic re-acceleration by plasma turbulence is not applicable in the wings of these sources. A combination of the rest of the two assumptions, that is, the injection spectral index is varying (Palma et al. 2000), and presence of a gradient in magnetic field across the source, together with curved electron energy spectrum (Blundell & Rawlings 2000) could explain each of these X-shaped sources individually, but a single model presently seems implausible.

6.3.2 Environments of X-shaped sources

It has also been argued that the X-shaped morphology is essentially a hydrodynamic phenomenon which is a result of supersonic or buoyant flow of radio plasma in an asymmetric gas distribution. Leahy & Williams (1984) and Worrall et al. (1995) argued that the X-shaped radio morphology is a result of strong backflow of material behind the terminal hotspots of radio galaxy jets and subsequent buoyant evolution of the wings. In this model, the lobes and the wings must have been supersonic at some time in the past, but are now evolving buoyantly. Capetti et al. (2002) hypothesized that the X-shaped morphology is a direct result of the supersonic expansion and/or inflation of the lobe into an elliptical atmosphere and that all radio galaxies in such environments should exhibit this phenomenon. In this scenario, both the lobes and the wings should be enormously overpressurized relative to the ambient medium (Kraft et al. 2005). Although inhomogeneous and incomplete, the sample of X-shaped sources show diverse spectral morphologies and a single model with similar dynamics of the backflow/buoyancy, jet velocities, density contrast between the jet and the ambient medium, temperature and density profile of the medium, and morphology of the ambient medium for these sources would be a challenge.

6.3.3 Existing formation models versus merger of two AGN

Lal & Rao (2005) proposed to use the low-frequency spectra at different locations in the source, to distinguish between the formation models for these sources. In the simplest picture, the low surface brightness wings would have an older population of the electrons and therefore should have steeper spectral index as compared to the active high surface brightness radio lobes. However, the two categories of sources, namely, sources showing the wings to be of flatter spectral indices as compared to the active lobes (category i)

and sources showing the wings and the active lobes to be of comparable spectral indices (category ii), listed above do not support this simple picture. Instead, the third category of sources, five out of the 12 sources, supports this picture. Furthermore, none of the models mentioned earlier support the radio results from the first two categories of sources. On top, each of these models has its own limitation, which is independent of our spectral results.

Begelman, Blandford & Rees (1980) first suggested the possibility that AGN might contain a massive binary black hole. The proposition is justified through the following points. (i) The nuclei of most galaxies contain a massive black hole, and (ii) galaxies often merge. More importantly, all radio images of the sample of Xshaped sources show the wings and the lobes to be embedded well into the base and argues in favour of unresolved, coalescing binary AGN systems. In order to understand if the X-shaped sources are indeed examples of unresolved binary AGN systems, with two pairs of jets associated with two unresolved AGNs, several methods have been suggested, for example, an indirect hint for the presence of binary AGN is using the HST to identify inwardly decreasing surface brightness profiles in the galaxy. We have re-analysed the archived snapshot HST data for 3C 52, 3C 136.1, 3C 223.1, 3C 315, 3C 403 and 3C 433. A close inspection of the deconvolved brightness profiles in each source does not suggest a centrally depressed, nearly flat core. But is this due to obscuration of the core by the dusty disc (de Koff 1996) needs to be followed with new deep images.

6.4 Do X-shaped sources form a single class?

Based on the GMRT results presented above, we conclude that earlier models do not explain the formation scenario for the X-shaped sources. Only viable model is the 'alternative' model, that is, the X-shaped sources consist of two pairs of jets, which are associated with two unresolved AGNs (Lal & Rao 2005). This 'alternative' model not only explains earlier observational results, but also explains our low-frequency spectral results. The proposition also supports the small number of X-shaped sources, as the frequency of merger of two field AGNs is small and is definitely smaller than the number of minor merger events. Hence, we believe that every X-shaped source consists of an unresolved binary AGN, giving two pairs of jets corresponding to two AGNs. Whether or not the central binary black hole can actually account for the formation of X-shaped radio galaxies mainly depends on the time-scales of shrinking of separation radii and final merging of the binary system. In other words, it critically depends on the evolution and the stability of the binary system (Begelman et al. 1980).

We suggest high-resolution, multifrequency, phase-referenced very long baseline interferometry (VLBI) imaging of X-shaped sources in order to determine the recent active jet and investigate if these sources are examples of resolved binary AGN systems (Sudou, Iguchi & Murata 2003; Rodriguez et al. 2006). In addition, we also suggest deep *HST* and *Chandra* images to detect binary supermassive black holes, and a search process using the images from the VLA NVSS (Condon et al. 1998) and FIRST (Becker, White & Helfand 1995) surveys with a goal of increasing the total number of X-shaped radio sources, thereby forming a homogeneous complete sample. Additional observational results and wisdom gained from it would allow us to understand these sources in a statistical manner.

7 CONCLUSIONS

We have presented the lowest-frequency images of the sample of X-shaped sources at 240 and 610 MHz, and our radio spectral results have been instrumental in testing the formation scenario of

these sources. The measurements presented here represent most of the data base that we require for rigorously testing and understanding the formation models of these sources. Based on our careful analysis and estimation of the possible systematic errors along with the integrated radio flux densities and the spectral indices from it at several locations across each of these sources, we show that these sources divide into following three categories.

- (i) Sources in which the wings are of flatter spectral indices than the active lobes, namely, 4C 12.03, 3C 223.1 and B1059+169.
- (ii) Sources in which the wings and the active lobes have comparable spectral indices, namely, 3C 192, B2 0828+32, 4C 48.29 and 3C 403.
- (iii) Sources in which the wings are of steeper spectral indices than the active lobes, namely, NGC 326, 3C 52, 3C 136.1, 3C 315 and 3C 433.

These GMRT results do not support earlier known formation models for the X-shaped sources. While it is equally probable that the three categories, (i), (ii) and (iii), of sources are unrelated to one another, a single model to explain these sources is a challenge. Currently, only possible model is our 'alternative' model, that is, the X-shaped sources consist of two pairs of jets, which are associated with two unresolved AGN (Lal & Rao 2005).

There is definitely a need to understand the proposed formation scenario for X-shaped sources and, hence, follow-up work is necessary. Future VLBI results together with deep *HST* and *Chandra* images and results from a larger homogeneous complete sample of X-shaped sources would be useful in constraining any possible formation model.

ACKNOWLEDGMENTS

We thank the staff of the GMRT who have made these observations possible. The GMRT is run by the National Centre for Radio Astrophysics of the Tata Institute of Fundamental Research. We also thank the anonymous referee for his/her prompt review of this manuscript and for comments that led to the improvement of this paper. DVL thanks R. Nityananda and M. Hardcastle for discussions and several useful comments. This research has made use of the NED, which is operated by the Jet Propulsion Laboratory, Caltech, under contract with the NASA, and NASA's Astrophysics Data System.

REFERENCES

Alexander P., 2002, MNRAS, 335, 610

Alexander P., Leahy J. P., 1987, MNRAS, 225, 1

Baars J. W. M., Genzel R., Pauliny-Toth I. I. K., Witzel A., 1977, A&A, 61, 99

Becker R. H., White R. L., Edwards A. L., 1991, ApJS, 75, 1

Becker R. H., White R. L., Helfand D. J., 1995, ApJ, 450, 559

Begelman M. C., Blandford R. D., Rees M. J., 1980, Nature, 287, 307

Black A. R. S., Baum S. A., Leahy J. P., Perley R. A., Riley J. M., Scheuer P. A. G., 1992, MNRAS, 256, 186

Blundell K. M., Rawlings S., 2000, AJ, 119, 1111

Burns J. O., Gregory S. A., Holman G. D., 1981, ApJ, 250, 450

Capetti A., Zamfir S., Rossi P., Bodo G., Zanni C., Massaglia S., 2002, A&A, 394, 39

Condon J. J., Cotton W. D., Greisen E. W., Yin Q. F., Perley R. A., Taylor G. B., Broderick J. J., 1998, AJ, 115, 1693

de Koff S., Baum S. A., Sparks W. B., Biretta J., Golombek D., Macchetto F., McCarthy P., Miley G. K., 1996, ApJS, 107, 621

Dennett-Thorpe J., Bridle A. H., Laing R. A., Scheuer P. A. G., 1999, MN-RAS, 304, 271

Dennett-Thorpe J., Scheuer P. A. G., Laing R. A., Bridle A. H., Pooley G. G., Reich W., 2002, MNRAS, 330, 609

Ekers R. D., Fanti R., Lari C., Parma P., 1978, Nat, 276, 588

Fanaroff B. L., Riley J. M., 1974, MNRAS, 167, 31P

Feretti L., Giovannini G., Gregorini L., Parma P., 1983, A&A, 126, 311

Ficarra A., Grueff G., Tomassetti G., 1985, A&AS, 59, 255

Gopal-Krishna, Biermann P. L., Wiita P. J., 2003, ApJ, 594, L103

Gower J. F. R., Scott P. F., Wills D., 1967, Mem.RAS, 71, 49

Gregory P. C., Condon J. J., 1991, ApJS, 75, 1011

Hardcastle M. J., Alexander P., Pooley G. G., Riley J. M., 1997, MNRAS, 288, 859

Heckman T. M., O'Dea C., P., Baum S. A., Laurikainen E., 1994, ApJ, 428, 65

Högbom J. A., 1979, A&AS, 36, 173

Kaiser C. R., Alexander P., 1997, MNRAS, 286, 215

Kaiser C. R., Alexander P., 1999, MNRAS, 305, 707

Kellermann K. I., Pauliny-Toth I. I. K., Williams P. J. S., 1969, ApJ, 157, 1

Kraft R. P., Hardcastle M. J., Worrall D. M., Murray S. S., 2005, ApJ, 622, 149

Kuhr H., Witzel A., Pauliny-Toth I. I. K., Nauber U., 1981, A&AS, 45, 367 Laing R. A., Riley J. M., Longair M. S., 1983, MNRAS, 204, 151

Lal D. V., Rao A. P., 2005, MNRAS, 356, 232

Large M. I., Mills B. Y., Little A. G., Crawford D. F., Sutton J. M., 1981, MNRAS, 194, 693

Leahy J. P., Parma P., 1992, in Roland J., Sol H., Pelletier G., eds, Extragalactic Radio Sources. From Beams to Jets. Cambridge Univ. Press, Cambridge, p. 307

Leahy J. P., Williams A. G., 1984, MNRAS, 210, 929

Leahy J. P., Black A. R. S., Denett-Thorpe J., Hardcastle M. J., Komissarov S., Perley R. A., Riley J. M., Scheuer P. A. G., 1997, MNRAS, 291, 20

Mack K.-H., Gregorini L., Parma P., Klein U., 1994, A&AS, 103, 157

Martel A. R. et al., 1999, ApJS, 122, 25

McCrathy P., Spinard H., van Breugel W., 1995, ApJS, 99, 27

Merritt D., 2004, in Ho L. C., ed., Coevolution of Black Holes and Galaxies. Cambridge Univ. Press, Cambridge, p. 263

Merritt D., Ekers R. D., 2002, Sci, 297, 1310

Murgia M., Parma P., de Ruiter H. R., Bondi M., Ekers R. D., Fanti R., Fomalont E. B., 2001, A&A, 380, 102

Owen F. N., Ledlow M. J., 1997, ApJS, 108, 41

Palma C., Bauer F. E., Cotton W. D., Bridle A. H., Majewski S. R., Sarazin C. L., 2000, AJ, 119, 2068

Parma P., Ekers R. D., Fanti R., 1985, A&AS, 59, 511

Pilkington J. D. H., Scott P. F., 1965, Mem.RAS, 69, 183

Rees M. J., 1978, Nat, 275, 516

Rodriguez C., Taylor G. B., Zavala R. T., Peck A. B., Pollack L. K., Romani R. W., 2006, ApJ, 646, 49

Rottmann H., 2001, PhD thesis, Rheinischen Friedrich-Wilhelms-Univesität Bonn

Ryle M., 1960, J. Inst. Electr. Eng., 6, 14

Sandage A., 1972, ApJ, 178, 25

Scheuer P. A. G., 1974, Sci, 300, 1263

Scheuer P. A. G., 1995, MNRAS, 277, 331

Steer D., Dewdney P., Ito M., 2003, Sci, 300, 1263

Sudou H., Iguchi S., Murata Y., 2003, Sci, 300, 1263

Swarup G., Ananthakrishnan S., Kapahi V. K., Rao A. P., Subrahmanya C. R., Kulkarni V. K., 1991, Current Science, 60, 95

Ulrich M.-H., Rönnback J., 1996, A&A, 313, 750

van Breugel W., Jägers W., 1982, A&AS, 49, 529

van Breugel W., Helfand D., Balick B., Heckman T., Miley G., 1983, AJ, 88 40

White R. L., Becker R. H., 1992, ApJS, 79, 331

Wirth A., Smarr L., Gallagher J. S., 1982, AJ, 87, 602

Worrall D. M., Birkinshaw M., Cameron R. A., 1995, ApJ, 449, 93

Zirbel E. L., 1997, ApJ, 476, 489

Zwicky F., Kowal C. T., 1968, Catalogue of Galaxies and Clusters of Galaxies. Caltech, Pasadena

This paper has been typeset from a TEX/LATEX file prepared by the author.